TR-AC-0020 010

Lateral Wet Oxidation of AlAs Layer in GaAs/AlAs Heterostructures Grown by MBE on GaAs (n11)A Substrates

Pablo O. Vaccaro

1998. 4.21

ATR環境適応通信研究所

要旨

Al_xO_yを化合物半導体量子効果デバイスへ応用するために、(n11)A GaAs 基板(n=1, 2, 3, 4)上にMBE(分子線エピタキシー)成長させたGaAs/AlAsヘテロ構造内におけるAlAs層の横方向酸化特性についての研究が行われている。まず、それぞれの面方向基板における酸化速度の方向依存性を390℃から510℃の間で測定した。そこで酸化速度には高い異方性が存在し、その異方性は結晶の対称性に関係していることがわかった。また酸化は酸化時間に対して初期段階ではリニア則に従って進み、徐々にパラボリック則に従うようになる。さらに酸化速度の温度依存性を390℃から600℃の間で測定した。酸化は390℃越えると観測でき、540℃を越えるとサンプルの表面に劣化が起きる。その劣化は、酸化反応によって生成される気体がエピ層の内部に圧力をかけるために起こると考えられる。光学的反射率計測結果が、今回生成された酸化膜が以前に報告されている酸化膜よりも均一な膜であることを示した。Al_xO_y-AlGaAs-GaAs DBRs(分布ブラッグ反射器)の反射スペクトルは理論的に予想された結果とほぼ同じであった。

-Abstract-

In order to obtain Al_xO_y layer for quantum device application, the lateral sidewall oxidation of AlAs layers grown by molecular beam epitaxiy (MBE) on GaAs (n11)A-oriented substrates (n=1, 2, 3, 4) within heterostructures was investigated. The time dependence of the oxidation rate was found to follow a linear law for the initial process, and later a parabolic law. The direction dependence of the oxidation rate for each type of substrate was measured between 390 and 510 ℃. It was found that the oxidation rate is highly anisotropic and that the anisotropy is related to the symmetry of the crystal structure. The temperature dependence of the oxidation rate was also measured between 390 and 600 ℃. Oxidation was observable for temperatures above 390 ℃ and the surface of the samples degraded when the temperature exceeded 540 ℃. The degradation seemed to be related to the build up of pressure inside the epilayers due to gases evoling from oxidation reaction. Optical reflection spectroscopic measurements suggested that oxidized layers are more compact than those reported previously. It was also found that Al_xO_y-AlGaAs-GaAs distributed bragg reflectors (DBRs) have reflectance spectra close to theoretically expected ones.

A Table of Contents

1 Introduction 1

2 Theoretical Background 3
2.1 Wet Oxidation 3
2.2 VCSELs and DBR 3
2.3 Optical Reflectivity of Multilayer Structures 4
2.4 Contact Resistivity 4

3 Experimental 6
3.1 Fabrication 6
3.1.1 Sample Preparation for Oxidation Rate Measurement and Optical Characteristics 6
3.1.2 Sample Preparation for Measurement of p Contact Resistance 7
3.2 Structure of the Samples and Details of the Process 7
3.3 Characterization 8
3.3.1 Substrate Orientation, Oxidation Direction, Temperature, and Time for Oxidation Dependence 8
3.3.2 Optical Reflectance Spectroscopy 8
3.3.3 p Contact Resistivity 8

4 Oxidation Mechanism 9
4.1 Time Dependence of Oxidation 9
4.2 Substrate Orientation and Oxidation Direction Dependence on Temperature 10
4.3 High Temperature Oxidation 12
4.4 Sealing of AlAs against Oxidation 13

5 Optical Characterization 14
5.1 Reflectivity Spectra 14
5.2 Analysis of DBR Structure 16

6 Electrical Characterization 18
6.1 p Contact 18
6.2 Al_xO_y Film for n, p Contact 18

7 Conclusion 20

Chapter 1

Introduction

The difficulty in forming high-quality native oxide layers on III-V semiconductors has been a disadvantage in fabricationg such devices, unlike silicon. Recently, however, interest has been in Al_xO_y layers obtained by the wet oxidation of AlAs for III-V semiconductors. These layers are expected to be applied to optical and electronic devices, because the fabrication procedure is relatively simple, and oxide layers have a good mechanical strength, good electrical insulating properties, and a low refractive index [1] [2]. For example, the above oxide layers can be used to fabricate MOSFET structures, index-guided lasers, Fabry-Perot microcavities, and planar waveguides with compound semiconductors [3]. Unfortunately, not much experimental data is available on the oxidation processes and oxide properties. None the less, it is important to have a considerable amount of data and a theoretical understanding of oxides before fabricating devices. This is because they will allow the assessment of the short, and long term reliability of such devices [4]-[6].

Crystal growth by MBE on GaAs (n11)A substrates is a subject that is also attracting considerable interest, and was investigated by K. Fujita and P. O. Vaccaro [7]. These substrates have some unique properties: 1) Both n- and p-type doping can be achieved by using silicon as a dopant, 2) A very high hole concentration can be obtained through silicon doping, 3) The light emission properties are better, and 4) The Piezoelectric effect with an electric field perpendicular to the layers can be observed by introducing strain. All of these properties open the possibility for fabricating devices with new capabilities.

Fabricating light emitting diodes, tunnel diodes, and tunnel transistors using the amphoteric doping properties of silicon on the above-mentioned high-index substrates was investigated by H. Ohnishi *et al.*[8] [9]. Vertical cavity surface emitting lasers (VCSELs) on GaAs (311)A substrates was investigated by M. Takahashi *et al.*[10]. VCSELs are generating intense interest as a light source for optical systems. Their advantages include simple integration into 2-D arrays, on-wafer testing, and optical disk memories, as well as efficient optical fiber coupling [11]. However, producing the high reflectivity mirrors (Al(Ga)As-distributed Bragg reflectors (DBR)) requires a long term growth, and ensuring that the peak gain wavelength and the vertical cavity resonance overlap requires a very strict tolerance on the thickness of the layers is very strict (within a few percent). On the other hand, Al_xO_y/GaAs DBRs have a high reflectivity with a few periods and a wide stop band, which reduces the phase sensitivity near

the cavity resonance.

Highly efficient VCSELs with a low threshold current and high optical confinement can be fabricated by using Al_xO_y/GaAs DBRs [12]-[16]. Before this can be done, it is necessary to study the electrical and optical properties, and to obtain a theoretical understanding of Al_xO_y/GaAs DBRs grown by MBE on high-index substrates.

In the present work, GaAs/AlAs heterostructures on GaAs (n11)A-oriented substrates were grown and investigating were made on the dependence on the substrate orientation, the oxidation direction, the temperature and the time necessary for the lateral oxidation of the AlAs layers. In addtion, Al_xO_y/GaAs DBRs were fabricated and their reflection characteristics were studied. It is shown that the center wavelength of DBRs can be adjusted during the oxidation process. Also we studied the preparation and annealing conditions for p-type contacts on GaAs, to be used in devices that include Al_xO_y layers. The sample structure and method of measurement to evaluate the electrical characteristics of Al_xO_y are shown.

The strucure of this thesis is as follows: theoretical background, experimental, oxidation rate, optical characterization, electrical characterization, and conclusion.

Chapter 2

Theoretical Background

2.1 Wet Oxidation

Al_xO_y layers are formed by *wet thermal oxidation* of AlAs through chemical reaction in a nitrogen and water vapor atmosphere. The expected reaction is represented by the following chemical fomula [4][5].

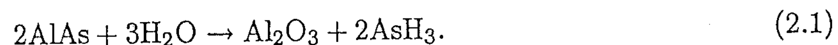

$$2AlAs + 3H_2O \rightarrow Al_2O_3 + 2AsH_3. \tag{2.1}$$

The equation shows that two molecules of AlAs react to form one molecule of Al_xO_y. The volume per "molecule" of AlAs, crystallized in a zinc blende structure (shown in Fig. 2.1) (lattice constant of 5.662 Å) is 45.4 $Å^3$. On the other hand, Al_xO_y in the γ-phase, crystallized with a cubic Fd3m spinel-like structure, consisting of 32 atoms of oxygen, $21\frac{1}{3}$ atoms of Al, and $2\ \frac{2}{3}$ vacancies per unit cube, has a cube edge of 7.9 Å. This corresponds to a volume of 46.2 $Å^3$ per molecule of Al_xO_y. Therefore, the reaction given by Eq. (2.1) implies a shrinkage of about 50% (by volume) in the AlAs layer if it is converted to compact γ-Al_xO_y.

2.2 VCSELs and DBR

Figure 2.2 shows a model of a Fabry Perot resonator in a VCSEL. The cavity is formed by the two surfaces of an epitaxial layer, and the light output is taken vertically from one of the mirror surfaces. The threshold density of this experimental VCSEL was rather high in comparison with a conventional stripe laser because of the short gain region and insufficient reflectivity of the mirror. From to preliminary research, the following points have been recognized to be particularly important for reducing the threshold current of VCSELs.

(1) High reflectivity of the laser mirrors ($R > 95\%$)

(2) An effective current confining structure.

As mirrors satisfying these conditions, DBRs have been suggested. Fundermental DBRs are composed of multi periodical layers of two ~~or three~~ materials where the refractive indexes differ

(e.g., AlGaAs and GaAs) by a quarter wavelength. Figure 2.3 shows a shematic drawing of a DBR and the light field intensity.

Fine growth technologies like MBE can produce superlattice structures that enable the fabrication of DBR-type VCSELs. For example, GaAs/AlAs DBRs are composed of over 30-layers of AlGaAs and GaAs with quarter wavelength spacing. The differences in the indexes between these materials are large, and the DBRs have a high reflectivity and a wide bandwidth [11].

2.3 Optical Reflectivity of Multilayer Structures

The reflectivity and transmissivity of a series of slabs of $Al_xGa_{1-x}As$ with x between 0 and 1, separated by abrupt plane boundaries, can be calculated using the transefer-matrix method. Fig. 2.4 shows the incident, reflected and transmitted light in one slab of material "1" with thickness d between slabs of materials "0" and "2". Since the tangential components of the electric and magnetic fields pararell to the boundaries are continuous can be equated at each interface "a" and "b", and characteristic matrix for each layer is obtained:

$$\begin{pmatrix} E_a \\ H_a \end{pmatrix} = \begin{pmatrix} \cos\delta_1 & i \cdot \sin\delta_1 / y_1 \\ iy_j \cdot \sin\delta_1 & \cos\delta_1 \end{pmatrix} \begin{pmatrix} E_b \\ H_b \end{pmatrix}, \tag{2.2}$$

where $y_1 = n_1 - i \cdot k_1$ is the optical admittance and $\delta_1 = 2\pi y_1 d_1 / \lambda_{light}$. The results can be extended to n-layers, and after rearrangement, the following equation is obtained:

$$\begin{pmatrix} B \\ C \end{pmatrix} = \prod_{j=1}^{n} \left(\begin{pmatrix} \cos\delta_1 & i \cdot \sin\delta_1 / y_j \\ iy_j \cdot \sin\delta_1 & \cos\delta_j \end{pmatrix} \right) \begin{pmatrix} 1 \\ y_{sub} \end{pmatrix}, \tag{2.3}$$

where $B = E_a/E_b$, $C = H_a/E_b$, and y_{sub} is the substrate's optical admittance. The reflection coefficient is calculated as:

$$R = \frac{(y_0 B - C)(y_0 B - C)}{(y_0 B + C)(y_0 B + C)}, \tag{2.4}$$

where y_0 is the optical admittance of the incidence media (typically, it is air).

The transmission coefficient is calculated as:

$$T = \frac{4 y_0 Re(y_{sub})}{(y_0 B + C)(y_0 B + C)}. \tag{2.5}$$

A multi-layer structure can be characterized by reflectivity spectrum measurement and comparison with a simulated spectrum based on this theory.

2.4 Contact Resistivity

As the term "contact resistance" implies, there is a resistance associated with the electrode interface contact. This is illustrated in Fig. 2.5 (a), which shows a slab of a semiconductor material having cross-section area S and length L. The contact covers each end of the slab. The resistance of the bulk semiconductor material from end to end is simply $\rho L/S$, where ρ is

the resistivity of the semiconductor. However, there is also a contact resistance, R_c, associated with each ohmic contact. Hence, the total measured resistance, R is:

$$R = 2R_c + \rho \frac{L}{S}. \tag{2.6}$$

The fundamental entity characterizing the resistance of the contact is the specific contact resistance, r_c, which is the contact resistance of a unit area for a current flow perpendicular to the contact, and which is in units of $\Omega - \mathrm{cm}^2$. For the geometry of Fig. 2.5 (a), r_c is simply

$$r_c = R_c S. \tag{2.7}$$

The basic technique used to measure the contact resistance of planar ohmic contacts employs a test pattern composed of differently spaced ohmic contacts, as illustrated in Fig. 2.5 (b). The ohmic contacts are formed on a semiconductor surface and separated by a distance of L. The contacts have a width, W, and the pattern is isolated to restrict the current flow to across the distance L. The resistance between two such contacts consists of the two contact resistances plus the resistance of the semiconductor layer between the two contacts. The latter resistance should depend only on the sheet resistance, the width of the contacts, and the distance between the contacts. Hence, the total (measured) resistance, R, is:

$$R = 2R_c + \frac{R_s}{W} L, \tag{2.8}$$

where R_s is the sheet resistance of the GaAs material between the ohmic contacts. R_c is the contact resistance.

Line fitting is done with:

$$R = a + bL, \tag{2.9}$$

where a Ω and b $\Omega/\mu\mathrm{m}$ are fitting constant,

and

$$\frac{dR}{dL} = \frac{R_s}{W} = b = \frac{\rho_s}{W \cdot d}. \tag{2.10}$$

Consequently,

$$\rho_s = b \cdot W \cdot d, \tag{2.11}$$

$$\rho_c = \frac{a}{2} \cdot W, \tag{2.12}$$

where ρ_s and ρ_c are the resistivity of the sheet and that of the contact, respectively. d is the layer thickness.

Chapter 3

Experimental

3.1 Fabrication

3.1.1 Sample Preparation for Oxidation Rate Measurement and Optical Characteristics

GaAs/AlAs heterostructures were grown on semi-insulating GaAs substrates with the following orientations : (100), (111)A5° off toward [100], (211)A, (311)A, and (411)A. We did not use GaAs (111)A just-oriented substrates because AlAs epilayers have a poor quality and tend to form a wurzite structure for this orientation. The native oxide layer was removed using H_2SO_4 and the wafers were rinsed in de-ionized water for 5 min. Subsequently the wafers were etched for 80 s with NH_4OH : H_2O_2 : H_2O (2:1:95) at 25 ℃. After the etching, the wafers were rinsed in de-ionized water for 5min. and dried with nitrogen jet. All of the samples were immediately mounted on molybdenum holders without indium and loaded into a Varian Modular Gen 2 molecular-beam-epitaxy (MBE) chamber. As beam equivalent pressure was 2.2×10^{-5} Torr and the As_4/Ga flux ratio was 6.5. After thermal cleaning at 700 ℃ for 5 min, a 200 or 300 nm GaAs buffer layer was grown at 620 ℃.

The sample structures prepared for oxidation are as follows: structure **A** consisted of single 10 nm GaAs surrounded by 10 nm $Al_{0.5}Ga_{0.5}As$ and separated by 100 nm AlAs, and a 50 nm GaAs cap layer (shown in Fig. 3.1 (a)). This structure is Fabry-Perot microcavity and fundamental strucuture of an AlAs-AlGaAs-GaAs DBR. Structure **B** (DBR structure) consisted nominally of five periods of 10 nm GaAs surrounded by 10 nm $Al_{0.5}Ga_{0.5}As$ and separated by 50 nm AlAs, and a 50 nm GaAs cap layer (shown in Fig. 3.1 (b)). Structure **C** consisted nominally of GaAs 40, 20, 10, 5, and 2.5 nm thick separated by 100 nm AlAs spacers, and an $Al_{0.5}Ga_{0.5}As$ cap layer (shown in Fig. 3.1 (c)).

Conventional photolithography and wet etching were used to pattern mesas on all of the samples. The mask patterns used in this study are shown in Fig. 3.2 (a) and (b).

The oxidation was carried out under a rapid thermal annealing even in an atmosphere of N_2 carrier gas (1 l/min.) bubbled through de-ionized water maintained at 90 ℃. A schematic drawing of the wet oxidation system and a sample after oxidation are showed in Fig. 3.3 (a) and (b), respectively. The annealing profile of the furnace used in the wet oxidation is shown in Fig. 3.4. The surface of all of the samples after oxidation was observed by optical microscopy.

3.1.2 Sample Preparation for Measurement of p Contact Resistance

GaAs (Si-doped) 520 nm thick, p-type layers were grown on semi-insulating GaAs (111)A just oriented substrates at 540 ℃, 570 ℃, and 600 ℃. The samples were patterned into mesas using the mask shown in Fig. 2.3 by conventional photolithography. Three type contacts were prepared by evaporation with a back pressure of 10^{-5} Pa, unnecessary metal were removed by lift off, and these samples were annealed at temperature and time shown in 3.4. The furnace used in this annealing is the same as used in oxidation.

3.2 Structure of the Samples and Details of the Process

The structure of the samples and the most relevant process conditions are described below.

(1) Samples **I**

- Growth structure: B
- Mask pattern: 200 μm stripes perpendicular to [110]
- Etchant: $H_2SO_4 : H_2O_2 : H_2O = 1:8:8$ at RT
- Oxidation conditions: continuous from 10 min to 70 min. (10 min. steps) at 410 ℃
- Measurement: time dependence

(2) Samples **II**

- Growth structure: A
- Mask pattern: Fig. 4 (a)
- Etchant: $H_2SO_4 : H_2O_2 : H_2O = 1:8:8$ at RT
- Oxidation conditions: 10 min at 390, 410, 430, 450 ℃ .
- Measurement: substrate orientation and oxidation direction dependence on temperature

(3) Samples **III**

- Growth structure: A
- Mask pattern: 100 μm stripes perpendicular to [110]
- Etchant: $H_2SO_4 : H_2O_2 : H_2O = 1:8:8$ at RT
- Oxidation conditions: 10 min. at 450, 480, 510, 540, 570, 600 ℃
- Measurement: substrate orientation and oxidation direction dependence on temperature

(4) Samples **IV**

- Growth structure: C
- Mask pattern: Fig. 4 (b)

- Etchant: $H_2SO_4 : H_2O_2 : H_2O = 1 : 8 : 8$ at RT
- Oxidation conditions: continuous and additional from 10 min to 60 min. (10 min. steps) at 380 ℃
- Measurement: time dependence

(5) Samples V

- Growth structure: B
- Mask pattern: 200 μm stripes perpendicular to [110]
- Etchant: $H_2SO_4 : H_2O_2 : H_2O = 1 : 8 : 8$ at RT
- Oxidation conditions: 60+50 min. at 410 ℃, 60 min. at 430 ℃, 30 min. at 450 ℃, 30 min. at 470 ℃, 20 min. at 490 ℃, complete oxidation
- Used measurement: optical reflectivity

(6) Samples VI

- Metals type and annealing condition
- Mn 20 nm / Au 300 nm: 1.5 min. at 380, 400, 420 ℃
- Zn 20 nm / Au 300 nm: 1.5 min. at 400, 430, 460 ℃
- Ti 500 nm / Pt 20 nm / Au 300 nm: 1.5 min. at 380, 420, 460 ℃

3.3 Characterization

3.3.1 Substrate Orientation, Oxidation Direction, Temperature, and Time for Oxidation Dependence

Oxidation lengths from the etched sidewalls were measured on samples **I**, **II**, **III**, and **IV**, with an optical microscope. The lateral oxidation rate data of the AlAs layers was organized accodingly to their dependence on the following parameters: substrate orientaiton, oxidation direction, temperature and time.

3.3.2 Optical Reflectance Spectroscopy

Optical reflectivity in the wavelength region from 400 nm to 1500 nm was measured in samples V. These measurements are performed with a spectrophotometer (Shimadzu Seisakujo. co. ltd.) in the reflectance mode. The reflected light intensity is measured by comparing to the reflected intensity from a calibrated mirror. The experimental spectra were compared to the results of simulated spectra calculated by the transfer matrix method (ref. 2. 2).

3.3.3 *p* Contact Resistivity

For samples VI, the resistance at each separation length was calculated by taking the I-V characteristics. After organizing the data, ρ_c and ρ_s of each contact were calculated by the theory shown in 2.3, the most suitable metals and annealing conditions for the p-contact in this work were required.

Chapter 4

Oxidation Mechanism

4.1 Time Dependence of Oxidation

Figure 4.1 shows a graph of the oxide thickness, r, of <110> on (111)A 5° off substrate were plotted from 10 to 70 min. This graph shows that the oxidation rate is fast for the initial process and becomes relatively slowler later. From this result, we can expect the oxidation rate to follow a linear law for the initial time controlled by interface reaction at the bulk-gas interface and a parabolic law for a large period of time by the diffusion of molecules. This idea of oxidation corresponds to the model of Si oxidation explained by A. S. Grove (shown in Fig. 4.9) [17]. The model is composed by the three fluxes corresponding to the three steps:

(1) Transporting flux, F_1, from the bulk of the gas to the oxide-gas interface.

(2) Diffusion flux, F_2, across the oxide already present.

(3) Reaction flux, F_3, at Si or AlAs surface.

The theoretical formula for the model is:

$$r^2 + Ar = B(t + \tau), \tag{4.1}$$

where

$$A \equiv 2D\left(\frac{1}{k_S} + \frac{1}{h}\right), \tag{4.2}$$

$$B \equiv \frac{2DC^*}{N_1}, \tag{4.3}$$

$$\tau \equiv \frac{r_i^2 + Ar_i}{B}. \tag{4.4}$$

D is the diffusivity of the oxidizing species in the oxide layer. k_S is the chemical surface-reaction rate constant for oxidation. h is the gas-phase mass-transfer coefficient in terms of the concentration in the solid. C^* is the partial pressure in the bulk of the gas. N_1 is the number of oxidant molecules. r_i is the thickness oxide layer grown in an earlier oxidation step.

Equation 4.1 can be solved for the oxide thickness as a function of time, resulting in:

$$r = \frac{A}{2}\left(\sqrt{1 + \frac{t+\tau}{A^2/4B}} - 1\right). \tag{4.5}$$

The experimental data were fitted by changing A, B, and τ in formula (4.5). The result of the fitting was very good, and it was also very good for the rest of the substrates with <110>. The result showed that this theory is additonally applicable to AlAs oxidation.

The formula (4.1) notes the two limiting cases of this general relationship.

For small times, i.e., $(t+\tau) \ll A^2/4B$, we obtain the liner law:

$$r = \frac{B}{A}(t+\tau), \tag{4.6}$$

where B/A is reffered to as the linear rate constant and is given by:

$$\frac{B}{A} = \frac{k_S h}{k_S + h}\frac{C^*}{N_1}. \tag{4.7}$$

This formula (4.7) shows the growth rate is determined by the k_S and h.

For large times, i.e., $t \gg A^2/4B$, the so-called parabolic relationship:

$$r^2 = Bt, \tag{4.8}$$

which is approached. In this relationship B is referred to as the parabolic rate constant. As shown in the formula (4.3), B is proportional to D:

$$B \propto D, \tag{4.9}$$

i.e., this formula means the growth rate is controlled by diffusion.

The value of r_i calculated by using the formula (4.4) where values of A, B, and τ, are the fitting constants, was approximately 20 nm. This is the thickness of the native oxide layer fromed by the wet etching. Judging from the experimental data, formation of this native oxide layer had almost no influence on the oxidation. Unfortunately the remaining physical constants could not be obtained in this work, because measurements under various conditions (the partial pressure in the bulk of the gas, the concentration of the oxidant, etc.) were inpossible. From now on, if these physical constants are able to be calculated by measuring more various conditions on the oxidation, the theory of the oxidation process will become clearer.

A linear growth-rate law indicated that the formed oxide film is porous, a parabolic law indicated that the oxide film is nonporous were reported [1] [3]. But, the result of our work can not be compared with earlier reports. Because material oxidized in these reports was AlGaAs, which is increasing activation energy as higher Ga content, is oxidized at relatively higher temperature (around 500 ℃)[2].

4.2 Substrate Orientation and Oxidation Direction Dependence on Temperature

As stated in the previous section (4.1), for the reason oxidation for short time is given by the formula (4.7), substrate orientaion and oxidation direction dependence wereexpected.

Figures 4.3 (a), (b), (c), (d), (e) and (f) show polar plots of the oxidation width for samples I grown on GaAs (100), (110), (111)A 5° off, (211)A, (311)A, and (411)A oriented substrates, respectively. The oxidation rate in the (100) surface is the fastest for a direction about 45° away from the natural cleaved direction <110>, as shown in Fig. 4.1(a). This direction is near the <100> direction, consequently, the shape of the graph is square where the four apexes stick out at 410 ℃. As shown in Fig. 4.1 (b), the <100> direction had the fastest oxidation rate for the (011) substrates. Figure 4.1 (c) shows roundish triangular shapes where the apex direction is $[2\bar{1}\bar{1}]$ 5° off toward $[0\bar{1}\bar{1}]$ for (111)A 5° off-oriented surface. For higher index surfaces, the anisotropy were observed even at lower oxidation temperature. The shape at 390 ℃ on (100) surface, however, was near circule and the anisotropy was weak.

From these graphs, we found that the oxidation rate is highly anisotropic and that the anisotropy becomes strong as the oxidation temperature increases.

When the surface is nearer to (100) (figures 4.3 (d), (e), and (f)), the oxide width of the apex direction becomes relatively short, and the shape of the graph becomes nearly trapezoidal. This transition of the shape from (100) to (111)A 5° off requires some rules on the oxidation rate. This expectation can be confirmed by results observed for sample surfaces oxidized at 480 ℃ (stated in the following).

On the surface of samples **II** oxidized at 480 ℃, The various shapes which depended on direction were formed by the lateral oxidation from holes (shown in Fig. 4.4). The holes were accidentally generated in the GaAs cap layer due to surface degradation by the high temperature, and the oxidation was started from one of these pin holes. The oxidation shapes observed on (100), (111)A 5° off, (311)A, and (411)A-oriented surface are similar to the shapes shown in figures 4.3 (a), (c), (e), and (f). In particular, the oxidation front shapes on the (100) surface show a four-fold crystal symmetry, and those on the (111)A 5° off surface show a three-fold crystal symmetry, in agreement with each crystal structure. However, the observed shapes on the surfaces of samples as shown in Fig. 4.4) are not indentical to the graph shapes shown in Fig. 4.3. The difference of the shapes between Fig. 4.3 and Fig. 4.4 is of the sharpness or convex nature of the edge and corner. This phenomenon is especially notable on the (100)-oriented surface. Supply and/or removal of H_2O and AsH_3 gas molecules for oxidation from pin holes are different from that of the stripes. By considering of the oxidation rate vector at the atomic scale, this can be explaned as follows. Let's assum that initial hole where the oxidation starts is approximately circular. First, the oxidation proceeds faster in the direction of large oxidation rate vector. As the result, the circular shape changes to anisotropy reoresented by the symmetry or structure of crystal.

From oxidation front shapes shown in Fig. 4.4, on the follwing orientations: $[0\bar{1}\bar{1}]$, $[2\bar{1}\bar{1}]$5° off, $[1\bar{1}\bar{1}]$, and $[2\bar{3}\bar{3}]$, we can see that oxidation rate largely changes with substrates orientation nearer to (100), an Arrhenius plot of the oxidation rate as a function of the inverse temperature is shown in Fig. 4.5. The temperature dependence of oxidation rate was evaluated by the data on the samples (**II** and **III**) oxidized from 390 to 510 ℃. Because the surface of the samples degraded over 510 ℃, there was no increase in the uniformity of the oxide film, the color observed with the optical microscope changed, and the exact oxidation width could not be measured. As shown in Fig. 4.5, on the oxidation rate, a very good agreement was obtained by line fitting. From these results, the activation energy, E_a on the oxidation (i.e., reaction at

the interface) to be determined using the law:

$$r = C\exp\left(-\frac{E_a}{k_B T}\right), \tag{4.10}$$

where C is a constant, k_B is Boltzman constant [2]. Figure 4.6 shows the activation energy on each of the oxidation direction. They shows that the activation energy increases as the oxidation direction approaches $[0\bar{1}\bar{1}]$ and that it is difficult for the oxidation to proceed to the direction, $[0\bar{1}\bar{1}]$. These results can be explained by the model shown in Fig. 4.5 where the top view is (111)A just-oriented in the zinc blende structure. The (111)A surface is not used in actual experiments, but simply to explain the idea that the surface is used. This idea shows as follows.

In the first process of oxidation, it is necessary to remove the As molecules from the AlAs structure. That is to say, a factor defining the oxidation rate on each direction is the strength of the covalent bond between the As and Al. It is expected for the oxidation rate to be represented by algebraic ideas. Concretely, the bonds almost perpendicular to $[0\bar{1}\bar{1}]$ number about three, and it is necessary for a large energy to cut the number of bonding. Rversibly there is only one bond that is almost perpendicular to $[2\bar{1}\bar{1}]$, and no large energy is necessary. These results and discussions confirm the idea that the oxidation process can be understood more clearly. In addition, they show that the oxidation rate also depends strongly on the crystal structure.

4.3 High Temperature Oxidation

The observation results for samples **III** oxidized at relatively higher temperatures (over 570 ℃) are stated in the following. On the surface of the (100) sample oxidized at 570 ℃, various geometric patterns appeared, as shown in Fig. 4.8 (a). The grooved pattern generated by strain between the fast and slow direction of oxidation rate was expected. This is because the anisotropy of the oxidation rate became much stronger at higher temperatures.

This grooved direction is in agreement with [100], i.e., the oxidation rate has much faster direction on the (100) surface, as shown in Fig. 4.8 (a). The direction of grooved line is opposite each other, and so grooves were taken place by a larger strain. Note that these patterns could only be observed on the inside about 20 μm from the etched sidewall. Figure 4.8 (b) shows the observed color of location that the grooves generates and not differs by optical interference. The difference in the observed color was mainly due to a change in the film thickness. For the reason that AsH_3 gas generated by the oxidation reaction pressure only inwards of the mesas, it is expected that this phenomenon takes place. This phenomenon could not be observed for lower temperature oxidation. This is explained as following.

In the oxidation process, it is necessary to transport H_2O molecules inward and AsH_3 gas outward. For oxidation at relatively lower temperatures, because the transport rate and the reaction rate balance each other out, the strain generated under this condition is not as large as that observed when grooving the crystal surface. Reversibly, at higher temperatures, the reaction rate is larger than the transport rate, the AsH_3 gas remains inward of the mesas, and large strain is generated. When the surface can not endure this strain, it grooves and the AsH_3 gas emittedfrom this groove. This was confirmed by the observation result of the (100) surface

oxidized at 600 ℃ (shown in Fig. 4.8 (c)). A larger groove took place inward of the mesas with a net shapes. This is because each groove became larger with increasing temperature. In Fig. 4.8 (a) as well, the line direction of the net agrees with [100].

In all of the (n11)A substrates oxidized at 600 ℃ (shown in figures 4.9 (a) and (b)), the same views were appeared. The observed color of the view was yellow from the etched sidewall to about 80 μm inward, and blue thereafter.This was expected to influence the change of the layer thickness and GaAs layer oxidation. In addition, the reason no groove took place on (n11)A as it did on (100) was because directions with a rapid oxidation rate are not opposite each other, this was expected.

4.4 Sealing of AlAs against Oxidation

In the previous section (4.1), the result of continuous oxidation about determinate time was shown. In this section, the result of additional oxidation at 380 ℃ are shown as compared to continuous oxidation. Here, "additional oxidation" means repeated periodical oxidation for a constant interval.

For the samples **IV**, figures 4.10 (a) and (b) show the continuous and additional oxidation rates at 380 ℃ plotted from 10 to 60 min, respectively. The anisotropy of the oxidation rate was not observed, because these samples were oxidized at relatively lower temperatures. The oxidation rates in the two figures are fitted by the theory stated in the previous section (ref. 2.1), a good agreement is obtained at 380 ℃. Comparing the two figures, no apparent can be seen. However, trend of oxidations for Figures 4.11 (a) and (b) (shown as follows) is different as explain as follows.

Figures 4.11 (a) and (b) shows the observed results with the optical microscope of sample surfaces oxidized under a continuous time and additional time. The view of both changes colors from the etched sidewall. As the reason for this color change, a non-existent AlGaAs layer between the GaAs and AlAs in the sample structure and a non-uniform oxide film. The AlGaAs layer relaxes the strain and the non-uniformity taking place in the oxidation.

Compared to the view of continuous oxidation shown in Fig. 4.11 (a), the view of additional oxidation shown in Fig. 4.11 (b) illustrates that the shows that clear line represented between the color and color, and the oxidation front is uneven. This unevenness indicates the sealing effect of the oxidation film. The effect presents that the oxide film generated by the first oxidation process prevents further oxidation from proceeding, as reported in [13]. The sealing effect is demonstrated through its use as a mask against wet oxidation in the fabrication of oxide-confined devices.

Chapter 5

Optical Characterization

5.1 Reflectivity Spectra

Figure 5.1 (a), (b), (c), (d), and (e) show the reflectivity spectra for samples V grown on GaAs (100), (111) A 5° off, (211)A, (311)A, and (411)A, respectively. In the following, # 0 shows a sample before oxidation, and #1, #2, #3, #4, and #5 show samples after oxidation at 410, 430, 450, 470, and 490 ℃, respectively. Data on oxidized samples add a compensation component that considers reflectivity of the GaAs exposed by etching. General trends for the substrate orientation of all of the samples are as follows.

There is the highest reflectivity (about 90%) peak of 730 nm in #0 spectra. This peak is called the "stop band", whose center wavelength and reflectance bandwidth determine the performance of DBRs. Reflectivity of stop band in #0 spectra is still low because it is necessary for DBR to have the reflectivity of stop band that is more than 95% (ref.2.2). Here, the reflectance bandwidth is defined as the wavelength range within which the reflectance is greater than 95%, and the center wavelength is defined as one of the stop bands. This wavelength range has high optical confinement. The center wavelength is actually a selective wavelength of DBRs made by the structure.

The center wavelength of the #1 spectra was 610 nm, and a blueshift of 120 nm from #0 was observed. This blueshift implied shrinkage of the total structure. Reflectivity of the stop band in the #1 spectra is neary 100% and the bandwidth is very wide (about 200 nm). This wider stop band could be observed at large differences in the refractive indexes between layer. It showed that the refractive index of AlAs ($\simeq$ 3) converts to one of Al_xO_y($\simeq$ 1.55), the structure used in this work has a high optical confinement DBR on the wavelength of approximately 600 nm, and a thinner DBR than an all-semiconductor DBR can be fabricated. The advantage of a thinner DBR includes a shorter epitaxitial growth times and a reduction in the absorption, scattering, and diffraction losses. A major benefit that follows from a wide bandwidth of an oxide-based DBR is a flatter phase response on the reflection, which relaxes the precise growth targets normally required to obtain high reflectivity in resonant cavity devices such as VCSELs [15]. In an earlier reports [14], the refractive index of Al_xO_y was found to be 1.55.

The spectra of #2 and #3 show blueshifts of approximately 10 and 20, respectively, from #1. These results can be expected from the degree of shrinkage on the Al_xO_y layer which becomes

large with increasing oxidation temperature. These spectra, from the samples oxidized at much higher temperatures (#4 and #5), show blueshifts exceeding 100 nm, several small peaks in the stop band, a lower total reflectivity. These results can be explained by each sample surface observed with an optical microscope, as shown in figures 5.1 (a), (b), and (c). The image of the oxidized part (shown in Fig. 5.2 (a)) has the same observed color and it shows that the oxidation film is uniform. However #4 and #5 in figures 5.2 (b) and (c), respectively, show the changing observed colors of the oxidized part as constant lengths from the etched sidewall. These color changes show that the oxidation film was not uniform to a large degree and the change of the film thickness changed digitally from the etched sidewall.

This is the reason the small peaks in the stop band exist were expected. We expected the small peaks to correspond to the variations in the film thickness. Because the reflected light was scattered by surface degradation for samples #4 and #5, we also expected the reflectivity to become lower. That to say, the moment the oxidation temperature exceeded 450 ℃, we expected the samples with the structure to show much lower characteristics like an optical mirror. From these results, we found that the temperature range able to generate a good oxide film, is from 400 to 450 ℃ and very limited.

In the next paragraph, the characteristics of spectra for (100) and (n11)A samples are shown.

(1) (100)

The reflectivity of #2 in the stop band was higher than that of #1 and #3, and a wider bandwidth covered the blueshift width of #3. On (100) substrates, the film oxidized at 430 ℃ had the highest optical reflectance coefficient. In the stop band of #4 and #5, small peaks existed at approximately 610, 520, and 450 nm. From this, we can expect the oxide film to have digital three-layer thickness.

(2) (111)A 5° off

The #1-#3 spectra that included the stop band generally showed reflectance characteristics, as stated in the previous paragraph. However, the stop band of the #4 and #5 spectra was slightly different from that of the other orientation samples, a hill with an apex at 600 nm existed.

(3) (211)A

The blueshifts of the #1-#3 spectra were constant wavelengths at the temperature steps. Such blueshits were not measured in the other samples, the oxide film on the (211)A substrate was expected to shrink proportionally to the oxidation temperature. The wavelength of the small peaks in the stop band of #4 and #5 corresponded to that of (100).

(4) (311)A

The reflectivity of the #1 spectra was generally lower than that of the #2 and #3 spectra. The wavelength of the small peaks in stop band of #4 and #5 corresponded to that of (100), as well as to that of (211)A.

(5) (411)A

The #1-#3 spectra including the stop band generally showed reflectance characteristics as stated in the previous paragraph. However, the reflectivity of the #4 and #5 spectra was much lower than that of the other orientation samples. The film was not expected to be more uniform than the others.

As shown above, though all of the samples were fabricated under the same conditions, the results of the reflectivity spectra were slightly different. This is because the anistropy of Al_xO_y is higher than that of AlAs. Therefore, to design DBRs on (n11)A substrates, it is necessary to consider these differences.

5.2 Analysis of DBR Structure

Figures 5.3 (a), (b), (c), and (d) show simulation results for a DBR structure. The structure of the samples oxidized at each temperature was analyzed based on these results. As shown in the #0 spectra, the measured data corresponded to the simulated data over the wavelength range as shown in Fig. 5.3 (a). At this time, the thickness of AlAs was 46 nm (design: 50 nm). The spectra from #1 to #3 were simulated by replacing the AlAs layers with other layers ($n = 1.55$) and changing the layer thickness. As in the previous chapter (ref. 2.1), at the time we expected the AlAs to convert Al_xO_y, as well as shrinkage of the oxide layer, as reported for the others. However the source of these variations could not be fully understood.

It is important to note that the determination of these variations is also influenced by the limited precision in the layer thickness measurement and simulation. First, on the assumption that AlGaAs is not oxidized, simulation was performed. However, to make the measured data correspond, more than 40% shrinkage of the Al_xO_y was needed. Actually, if such a large shrinkage in the structure takes place, destruction of the sample can be expected. In these samples, however, no destruction was not observed with the optical microscope and expected results were obtained from the reflectivity spectra. Therefore, based on the assumption that AlGaAs becomes thin as oxidation proceeds, simulation was performed in the same manner, and a relatively good agreement was obtained as shown in Fig. 5.3 (a). That is to say, the oxidation was expected to proceed not only laterally but also vertically. However, for the reason that the oxidation of $Al_xGa_{1-x}As$ became difficult with increasing Ga content (i.e. $x \to 0$)[2], the velocity of the vertical oxidation was much smaller than that of the lateral oxidation. In addition, as reported in [12], with further oxidation, the vertical oxidation began after complete oxidation of the AlAs layer. However, the measured data and simulated data in figures 5.3 (b), (c), and (d) show agreement on the whole. Therefore, we expected that in the continuous oxidation, both lateral oxidation and vertical oxidation would take place with increasing oxidation temperature, and lateral oxidation would take place with a faster vertical oxidation rate. Furthermore, conversion to Al_xO_y and a high-quality film in the region of the stop band was confirmed by these spectra. Two spectra, however, were not completely in agreement, i.e., the results of #0. We expected the reason for the lack of agreement to be that the refractive index of Al_xO_y changed on the frequency. This is because in this simulation, the index of Al_xO_y was constant.

The structures were analyzed and predicted by accurate fitting for the peak and valley at nearly 800 nm. In the first simulation, only the Al_xO_y thickness was used as a fitting parameter.

For the corresponding surface orientation, the optical length of Al_xO_y plotted at the oxidation temperature is shown in Fig. 5.4. The optical length is the product of the refractive index and the layer thickness. The thickness of AlGaAs was constant and equal to 29 nm. This figure shows that the degree of shrinkage becomes larger by increasing the oxidation temperature. However, the shrinkage rate at 450 ℃ oxidation is approximately 67% the average of the corresponding orientation sample, we expected that its value would be very large. In the second simulation, on the condition that the thickness of Al_xO_y was constant and equal to 39 nm (this value is the one at 410 ℃ and shows 84% shrinkage), fitting for the experimental data was performed by making the AlGaAs thickness thin. This condition included the shrinkage of Al_xO_y, because the rate of Al_xO_y generated by converting the AlGaAs is large in the oxide layer. The result of this simulation showed a good agreement, too. The AlGaAs thickness was from 29 to 26 nm and the shrinkage of the oxide generated by converting the AlAs layer was approximately from 84% to 78%. This result showed that the vertical oxidation rate becomes fast with increasing oxidation temperature. This shrinkage value is smaller than that of the first simulation, this idea seems plausible for this oxidation, but there has been no confirmation. This shrinkage was exoected to still be large and to cause strain in the structure. The strain made the GaAs active region surrounded by the mirror degrade. To relax the strain, it is necessary to improve the structure. For example, a larger Ga content and AlGaAs thickness are expected. The result that the optical length could be changed by the oxidation temperature showed that when an oxidation film is actually fabricated, the center wavelength of the DBR can be controlled by the oxidation temperature. In Fig. 5.4, the shrinkage trend slightly differs for each orientation sample. These slight differences are not understood as fitting errors or characteristics of the indivdual orientation samples. Therefore, it is necessary to eliminate the frequency dependence of the refractive index.

Chapter 6

Electrical Characterization

6.1 *p* Contact

The I-V characteristics of each contact before and after annealing using Mn/Au, Ti/Pt/Au, and Zn/Au electrodes are shown in figures. 6.1 (a), (b), and (c), respectively. Comparing the three figures after annealing, the I-V characteristics of the Zn/Au contact show the best linearity, and a larger current. The resistance on the contact separation length for each p type contact at various annealing temperatures are shown in figures 6.2 (a), (b), and (c). This is because Mn/Au and Ti/Pt/Au contacts are not very linear as shown in the I-V characteristics, figures separated by the applied voltage. ρ_s and ρ_c calculated by the theory described in 2.3 are shown in Table 6.1. The ρ_c of Zn/Au was the lowest value among the three types of contacts, besides the contact annealed at 460 ℃ had the lowest value. The ρ_s of that was constant on the whole the against annealing temperature. Therefore, in this work, the result that the Zn/Au metals annealed at 460 ℃ were the most suitable to the p contact was obtained experimentally. In the future, by utilizing this p contact to various devices, we expect improvements in the device quality.

6.2 Al_xO_y Film for *n*, *p* Contact

The sample structure and method will be considered to evaluate the descrived electrical characteristics of Al_xO_y as a future subject.

The structure grown by MBE will consist of single AlAs (non-doped) surrounded by a AlGaAs (n or p-doped) and GaAs (n or p-dope) cap layer (shown in Fig. 6.3). Some square with a different size will be patterned. The AlAs layer will be completely oxidized and n or p type contacts will be evaporated on the top and sidewall of the mesas. In the first step, concerning the fabrication of this sample, it will be necessary to determine the substrate orientation, oxidation conditions annealing conditions, etc.

In the second step (I-V measurement), when the I-V characterization is measured for this sample, the measured current, I will be expected to have two values: a bulk current, I_B, and a leakage current of outside mesas, I_L. This idea is presented as follows.

$$I = I_B + I_L = al^2 + bl \tag{6.1}$$

$$I_B \propto l^2 \tag{6.2}$$

$$I_L \propto l \tag{6.3}$$

where l is a side of the square. Many lattice defects are expected in the oxide film and the carrier will pass these lattice defects. Therefore I could be consider as a function l. The electrical constants (σ, ε, etc.) of Al_xO_y will be calculated by the measured results.

In addition, the current values for the layer thickness of Al_xO_y will indicate whthere the resistance is linear or not and whether the tunneling current exists or not.

Chapter 7

Conclusion

For the purpose of achieving highly efficient VCSELs using Al_xO_y/GaAs DBRs, oxidation mechanisms and the optical and electrical properties of the oxide layer have been investigated.

The experimental data concerning the time dependence of the oxidation rate was very well fitted by a theoretical formula based on an Si oxidation model. Our new theory applicable to AlAs oxidation and is very useful for determining suitable oxidation times in the oxide film fabrication.

The oxidation rate is highly anisotropic. We found that the anisotropy is related to the strength of the As bond and that the anisotropy could be explained by the crystal symmetry of the zinc blende structure.In the future, when the oxide film can be fabricated on (n11)A substrates, consideration will be needed on this anisotropy.

Over 540 ℃, the degradation seems to be related to the build up of pressure inside the epilayers due to gases that evolve from oxidation reaction.

From the results of reflectivity measurements, structures including Al_xO_y films were found to have high optical confinement and performance as DBRs. The oxidation temperature region in which a good oxide film could be obtained was from 400 to 450 ℃ and was very limited. The spectra of the oxide-based DBR on an (n11)A substrate will become important in the for design of optical devices, especially VCSELs on (n11)A substrates in the future. The spectra show blueshifts with increasing oxidation temperature. Actually, at the time the oxidation film was fabricated in this work, the selective wavelength could be controlled by the oxidation temperature. The reason is because two phenomena where present: the degree of shrinkage for the Al_xO_y film became large and the vertical oxidation proceeded to the AlGaAs layer.

Suitable metal types and annealing conditions for the p contact were found to be Zn/Au and 460 ℃, this was experimentally confirmed. In addition, the idea and method for evaluating the electrical characteristics of the Al_xO_y film were described. Based on this idea, the most suitable conditions and electrical characteristics of the oxide film for an n or p contact and bulk, need to be evaluated by the accumulation of experimental data.

These investigations will be very useful for achieving of various optical and electrical devices with a high quality and coefficient in the future.

Acknowledgments

This work was realized in collaboration with Mr. Kazuhisa Koizumi, from the Department of Electrical Engineering, Doshisha University, and this report was presented as a thesis for his Master degree. I wish also to acknowledge the collaboration of Prof. Tadashi Ohachi, from the Department of Electrical Engineering, Doshisha University, who was Mr. Koizumi's advisor throughout this work.

Bibliography

[1] R. S. Burton and T. E. Schlesinger: J. Appl. Phys. 76 (9), 5503 (1994).

[2] H. Nickel: J. Appl. Phys. 78 (8), 5201 (1995).

[3] F. A. Kish, S. A. Maranowski, G. E. Höfler, N. Holonyak, Jr., S. J. Caracci, J. M. Dallesasse, and K. C. Hsieh: Appl. Phys. Lett. 60 (25), 3165 (1992).

[4] S. Guha, F. Agashi, B. Pezeshki, J. A. Kash, D. W. Kisker, and N. A. Bojarczuk: Appl. Phys. Lett. 68 (7), 906 (1996).

[5] R. D. Twesten, D. M. Follstaedt, K. D. Choquette, R. P. Schneider, Jr.: Appl. Phys. Lett. 69 (1), 19 (1996).

[6] S. S. Shi, E. L. Hu, J. P. Zhang, Y. I. Chang, P. Parikh, and U. Mishra: Appl. Phys. Lett. 70 (10), 1923 (1996).

[7] K. Fujita and P. O. Vaccaro: Current Topics in Crystal Growth, 3 (1997) 1.

[8] H. Ohnishi, M. Hirai, K. Fujita, and T. Watanabe: J. J. Appl. Phys. vol.35, 1168 (1996).

[9] H. Ohnishi, M. Hirai, K. Fujita, and T. Watanabe: J. J. Appl. Phys. vol.36, 1853 (1997).

[10] M. Takahashi, P. O. Vaccaro, T. Watanabe, T. Mukaihara, F. Koyama, and K. Iga: Jap. J. Appl. Phys 35, 6102 (1996).

[11] G. A. Evans and J. M. Hammer: "Surface Emitting Semiconductor Lasers and Arrays" p. 72-107.

[12] M. H. MacDougal and P. D. Dupkus: IEEE Photo. Tech. Lett. 9(7), 884 (1997).

[13] D. H. Lim, G. M. Yang, J. H. Kim, K. Y. Lim, and H. J. Lee: Appl. Phys. Lett. 71 (14), 1915 (1997).

[14] M. H. MacDougal, H. Zhao, P. D. Dupkus, M. Ziari, and W. H. Steier: Electron. Lett., 1994, vol. 30, pp. 1147.

[15] M. H. MacDougal, S. G. Hummel, P. D. Dupkus, H. Zhao, and Y. Cheng: IEEE Photo. Tech. Lett. 7 (4), 385 (1995).

[16] M. H. MacDougal, G. M. Yang, A. E. Bond, C. K. Lin, D. Tishinin, and P. D. Dupkus: IEEE Photo. Tech. Lett. 8 (3), 310 (1995).

[17] A. S. Grove: "Physics and Technology of Semiconductor Device" p. 22.

List of Figures and Tables

- Fig. 2.1 Unit cell of a zinc blende structure.
- Fig. 2.2 Schematic drawing of a VCSEL.
- Fig. 2.3 Schematic drawing of a DBR and the light field intensity.
- Fig. 2.4 Reflection and transmission of a dielectric slab.
- Fig. 2.5 (a) A slab of material with ohmic contacts at the two ends, which exhibits a resistance composed of the end-to-end resistance of the material, plus two contact resistances.
- Fig. 2.5 (b) Basic pattern used to experimentally determine contact resistance parameters. The ohmic contacts are separated by increasing distances.
- Fig. 3.1 (a) Schematic drawing of structure A.
- Fig. 3.1 (b) Schematic drawing of structure B.
- Fig. 3.1 (c) Schematic drawing of structure C.
- Fig. 3.2 (a) Mask pattern (i).
- Fig. 3.2 (b) Mask pattern (ii).
- Fig. 3.3 (a) Schematic drawing of a wet oxidation system.
- Fig. 3.3 (b) Schematic drawing of a sample after oxidation.
- Fig. 3.4 The annealing profile of the furnace.
- Fig. 4.1 Time dependence of oxidation thickness (at 410 ℃, [110]).
- Fig. 4.2 Model for the thermal oxidation of Si or AlAs.
- Fig. 4.3 Polar plots of oxidation width dependence on the direction and the temperature.
  - (a) (100) surface.
  - (b) (110) surface.
  - (c) (111)A 5° off toward [100] surface.
  - (d) (211)A surface.

– (e) (311)A surface.
– (f) (411)A surface.

- Fig. 4.4 Top views of surfaces oxidized at 480 ℃ in samples **III** with an optical microscope.
- Fig. 4.5 Arrhenious plot of the oxidation rate as a function of the inverse temperature for each direction.
- Fig. 4.6 Activation energy on the oxidation proceeding along the direction toward the $[0\bar{1}\bar{1}]$ azimuth.
- Fig. 4.7 Schematic drawing of a zinc blende structure seen from (111)A just-oriented.
- Fig. 4.8 Top views of (100) surfaces oxidized over 570 ℃ with an optical microscope.
  – (a) Oxidized at 570 ℃ (× 1000).
  – (b) Oxidized at 570 ℃ (× 500).
  – (c) Oxidized at 600 ℃ (× 250).
- Fig. 4.9 Top views of (n11) surfaces oxidized at 600 ℃ with an optical microscope.
  – (a) (111)A 5° off surface.
  – (b) (211)A, (311)A, and (411)A surfaces.
- Fig. 4.10 Time dependence of oxidation thickness (at 380 ℃).
  – (a) Continuous oxidized.
  – (b) Additional oxidized.
- Fig. 4.11 Top views of (311)A surfaces oxidized at 380 ℃ with an optical microscope.
  – (a) Continuous oxidation.
  – (b) Additional oxidation.
- Fig. 5.1 Reflectance spectra for 5-period GaAs-AlGaAs-AlAs or oxide DBR structure.
  – (a) (100) surface.
  – (b) (111)A 5° off surface.
  – (c) (211)A surface.
  – (d) (311)A surface.
  – (e) (411)A surface.
- Fig. 5.2 Top views of a DBR (411)A surfaces completely oxidized in samples **V** with an optical microscope.
  – (a) Oxidized at 410 ℃.
  – (b) Oxidized at 470 ℃.

  - (c) Oxidized at 490 ℃.

- Fig. 5.3 Simulation results.
  - (a) Before oxidation.
  - (b) Oxidized at 410℃.
  - (c) Oxidized at 430℃.
  - (d) Oxidized at 450℃.

- Fig. 5.4 Optical length of Al_xO_y on the oxidation temperature.

- Fig. 6.1 I-V characteristics of p-type GaAs with a three-type contact.
  - (a) Mn/Au.
  - (b) Ti/Pt/Au.
  - (c) Zn/Au.

- Fig. 6.2 Resistance on the contact separation length.
  - (a) Mn/Au.
  - (b) Ti/Pt/Au.
  - (c) Zn/Au.

- Table. 6.1 Contact and sheet resistivity.

- Fig. 6.3 Electrical evaluation of Al_xO_y.

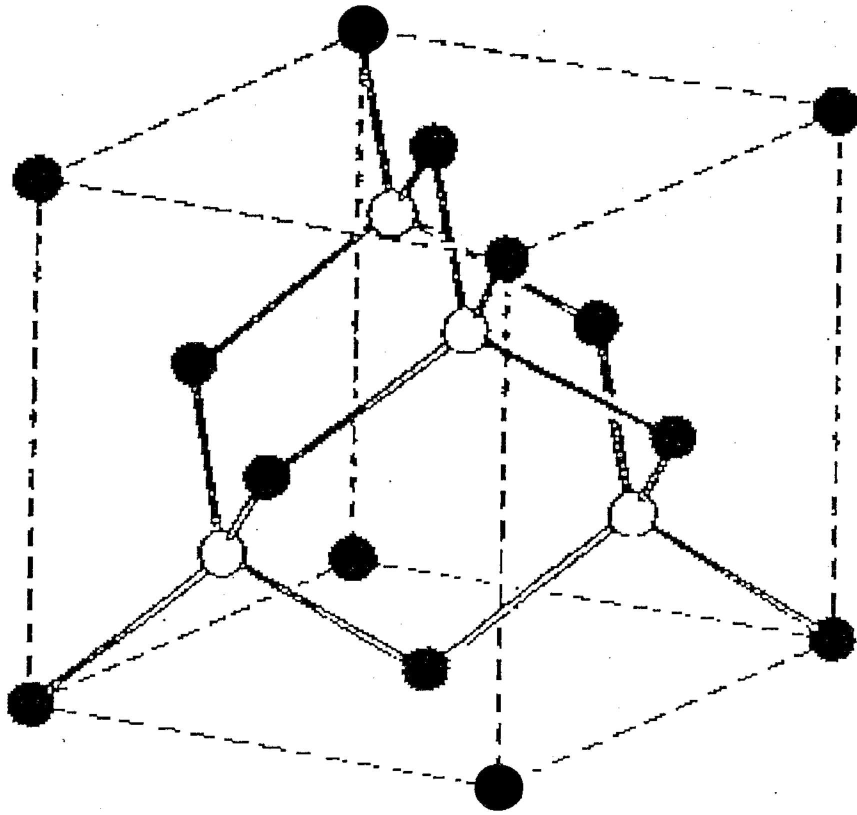

● III group atomic

○ V group atomic

Fig. 2.1 Unit cell of a zinc blende structure (AlAs, GaAs etc.).

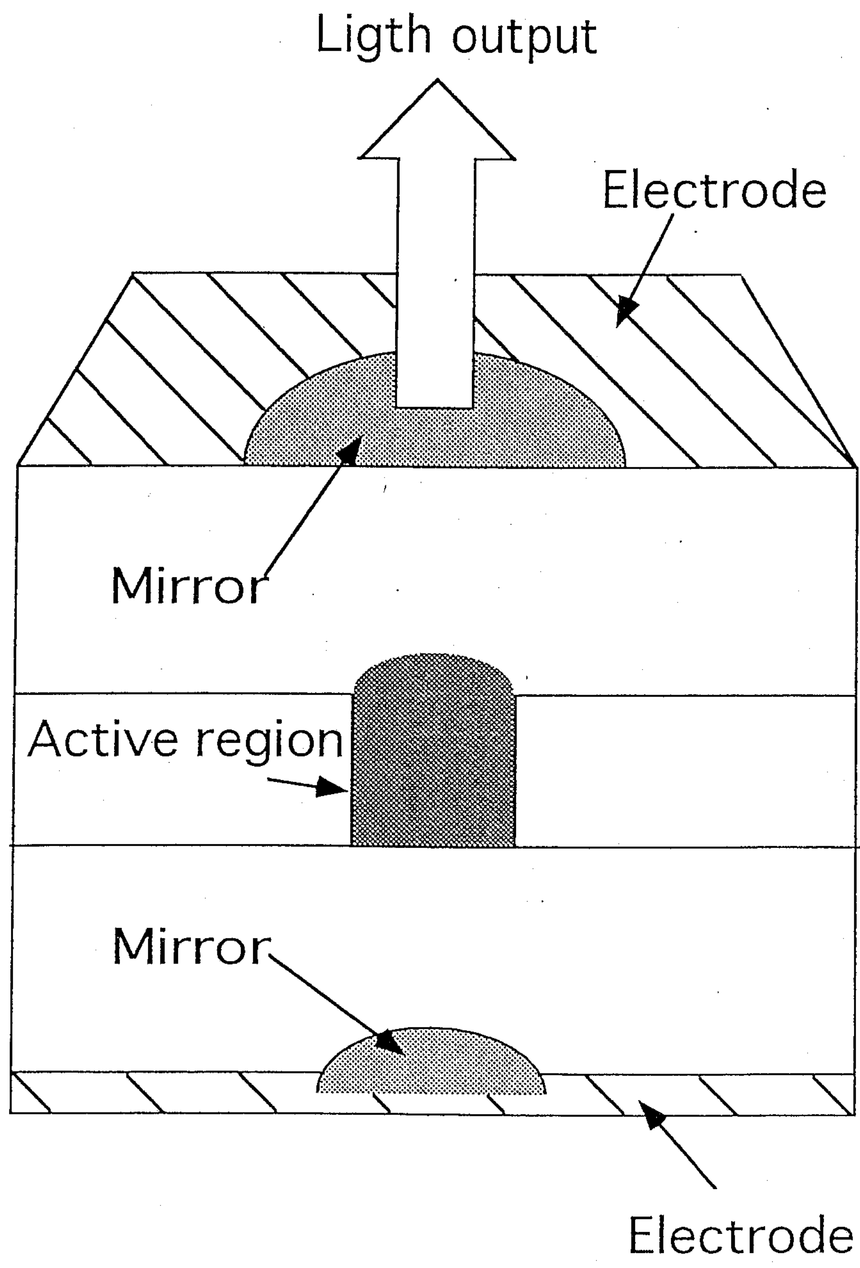

Fig. 2.2 Schematic drawing of a VCSEL.

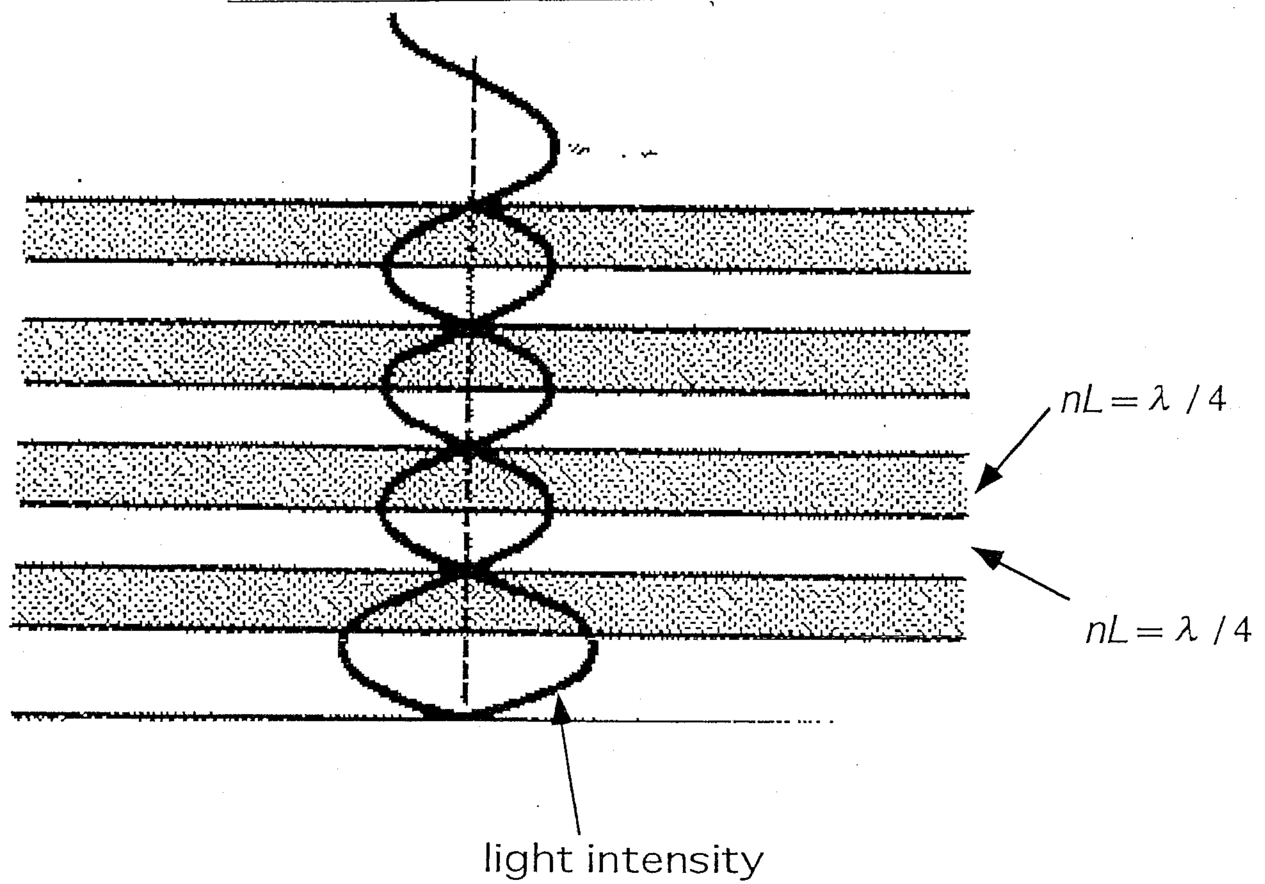

Fig. 2.3 Schematic drawing of a DBR and the light field intensity.

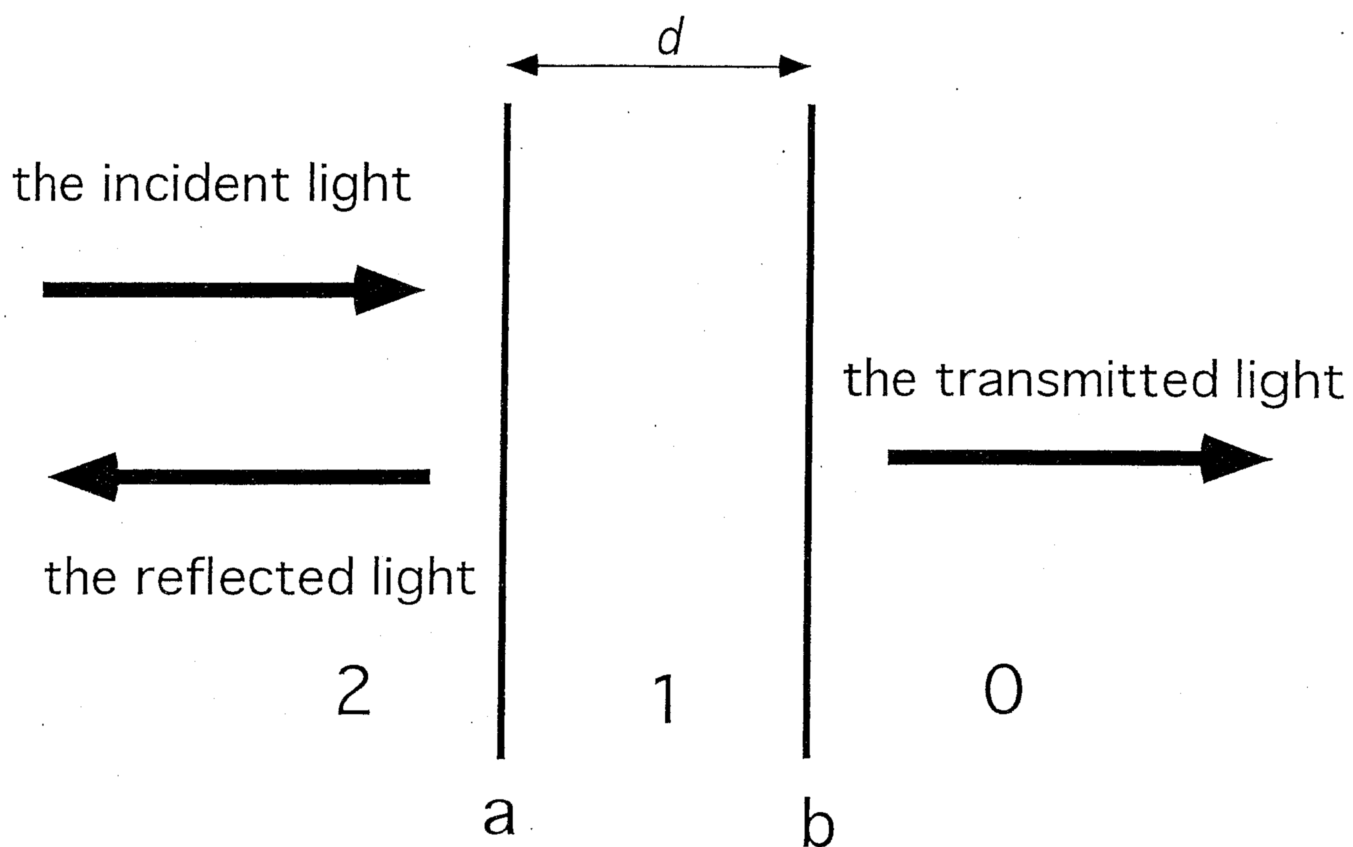

Fig. 2.4 Reflection and transmission of light in a dielectric slab.

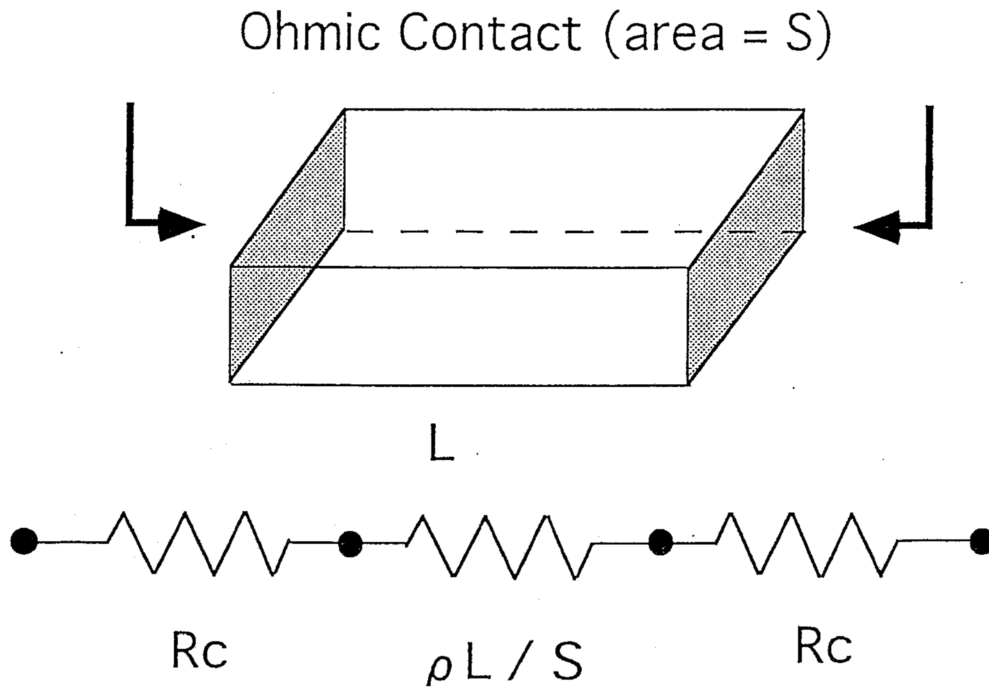

Fig. 2.5 (a) A slab of material with two Ohmic contacts.

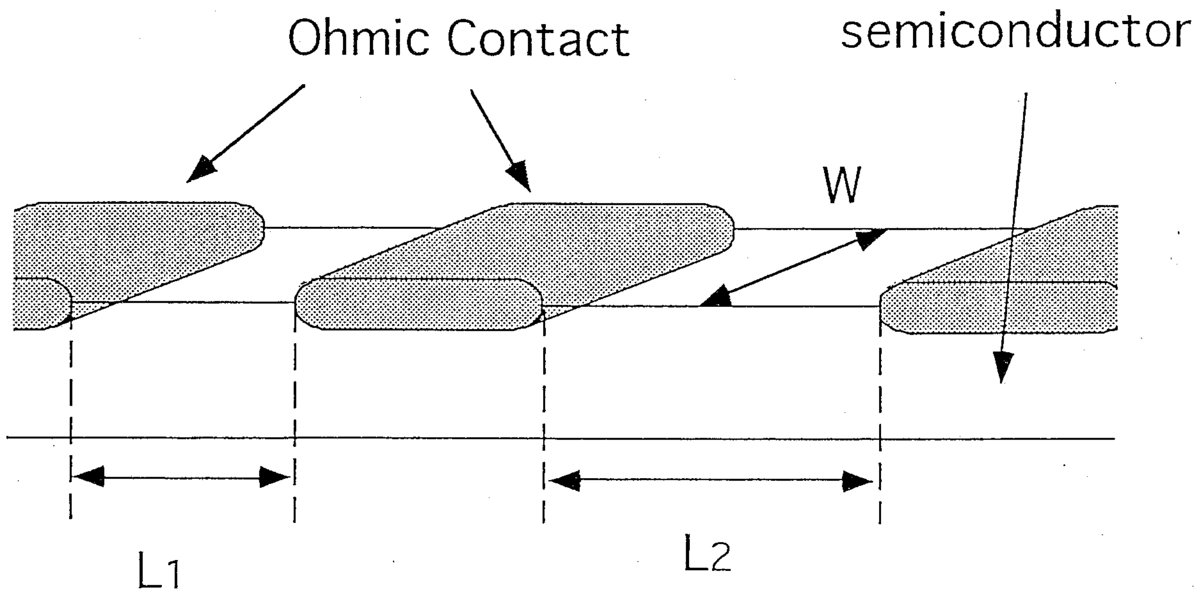

Fig. 2.5 (b) Basic pattern used experimentally determine contact resistance parameters.

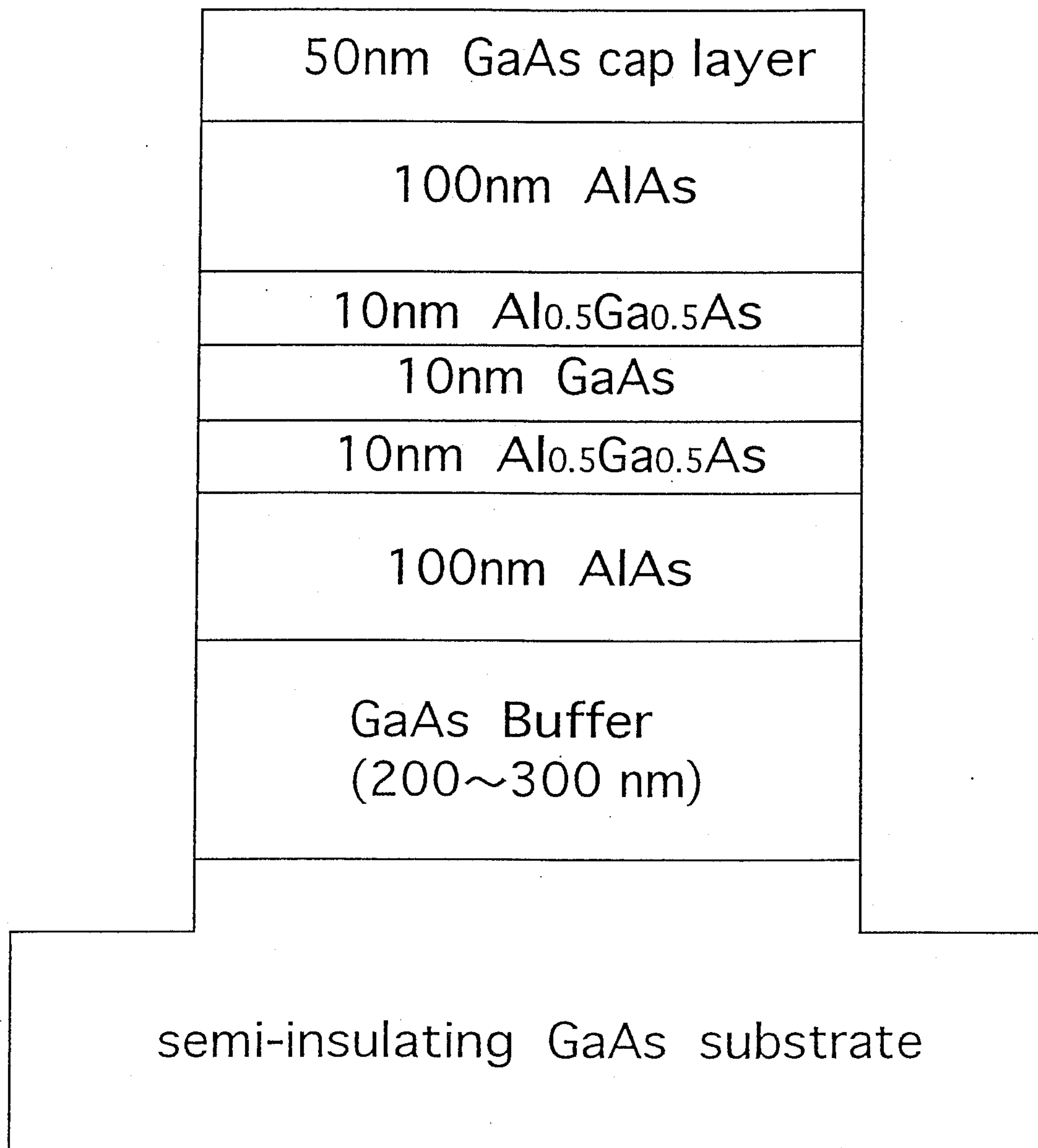

Fig. 3.1 (a) Schematic drawing of structure A.

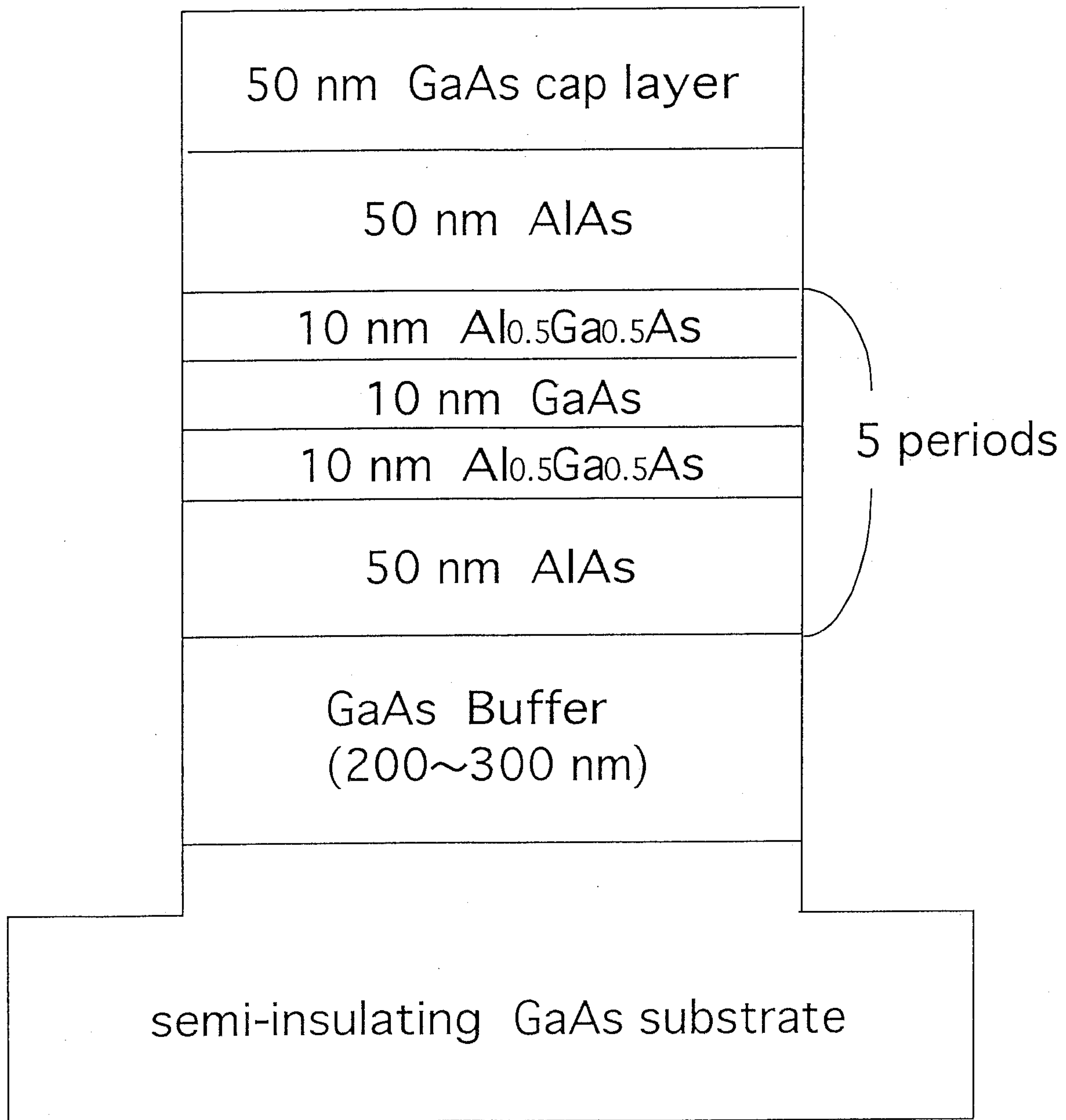

Fig. 3.1 (b) Schematic drawing of structure B.

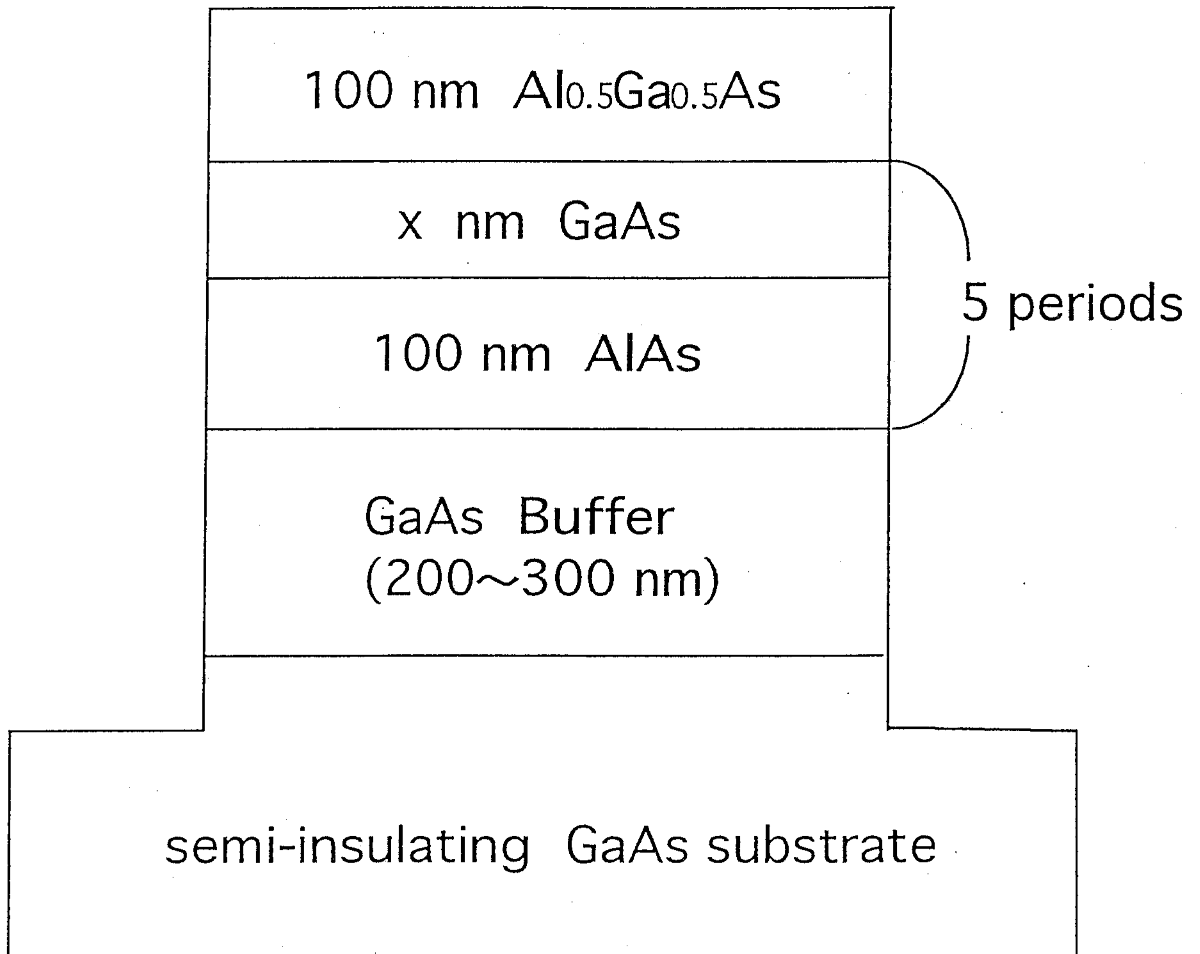

x = 40, 20, 10, 5, and 2.5

Fig. 3.1 (c) Schematic drawing of structure C.

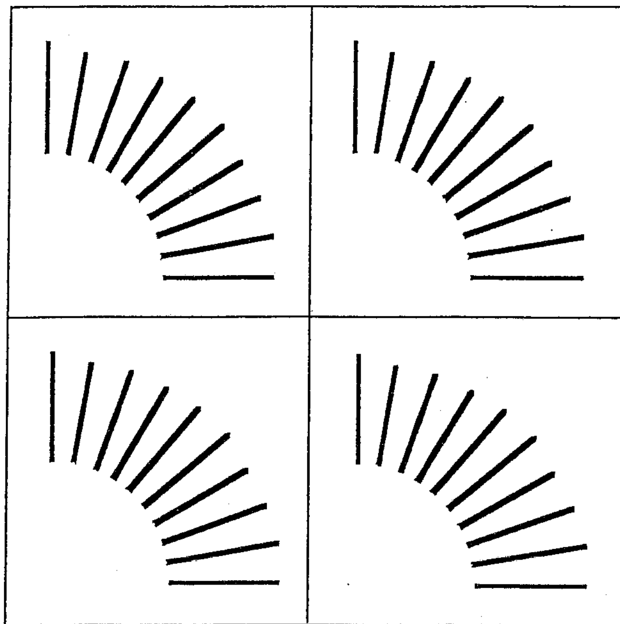

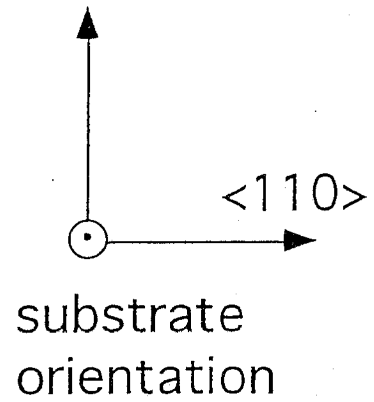

(a) mask(i).

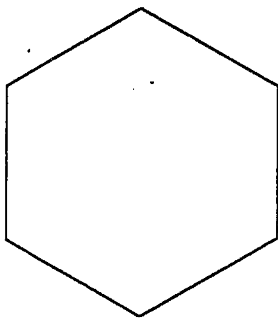

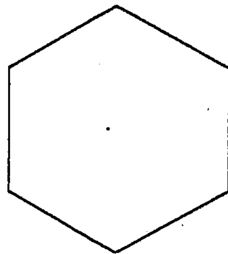

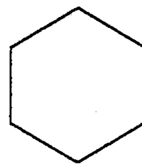

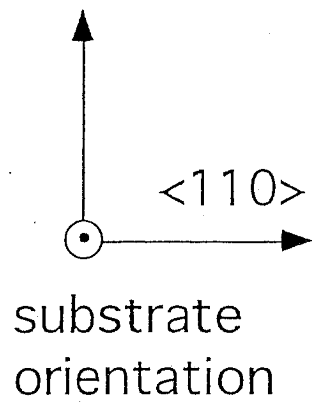

(b) mask(ii).

Fig. 3.2 Mask pattern.

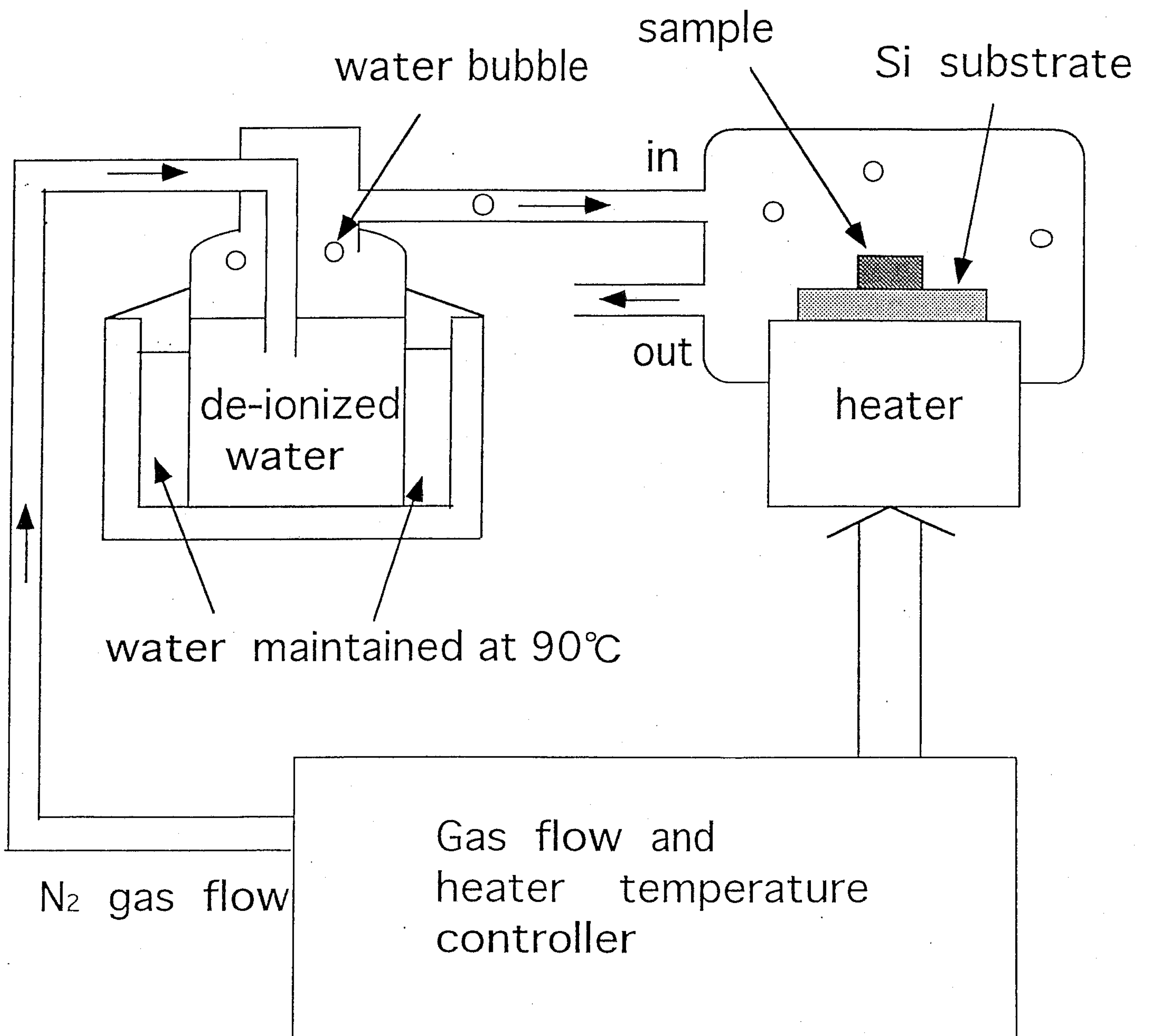

Fig. 3.3 (a) Schematic drawing of a wet oxidation system.

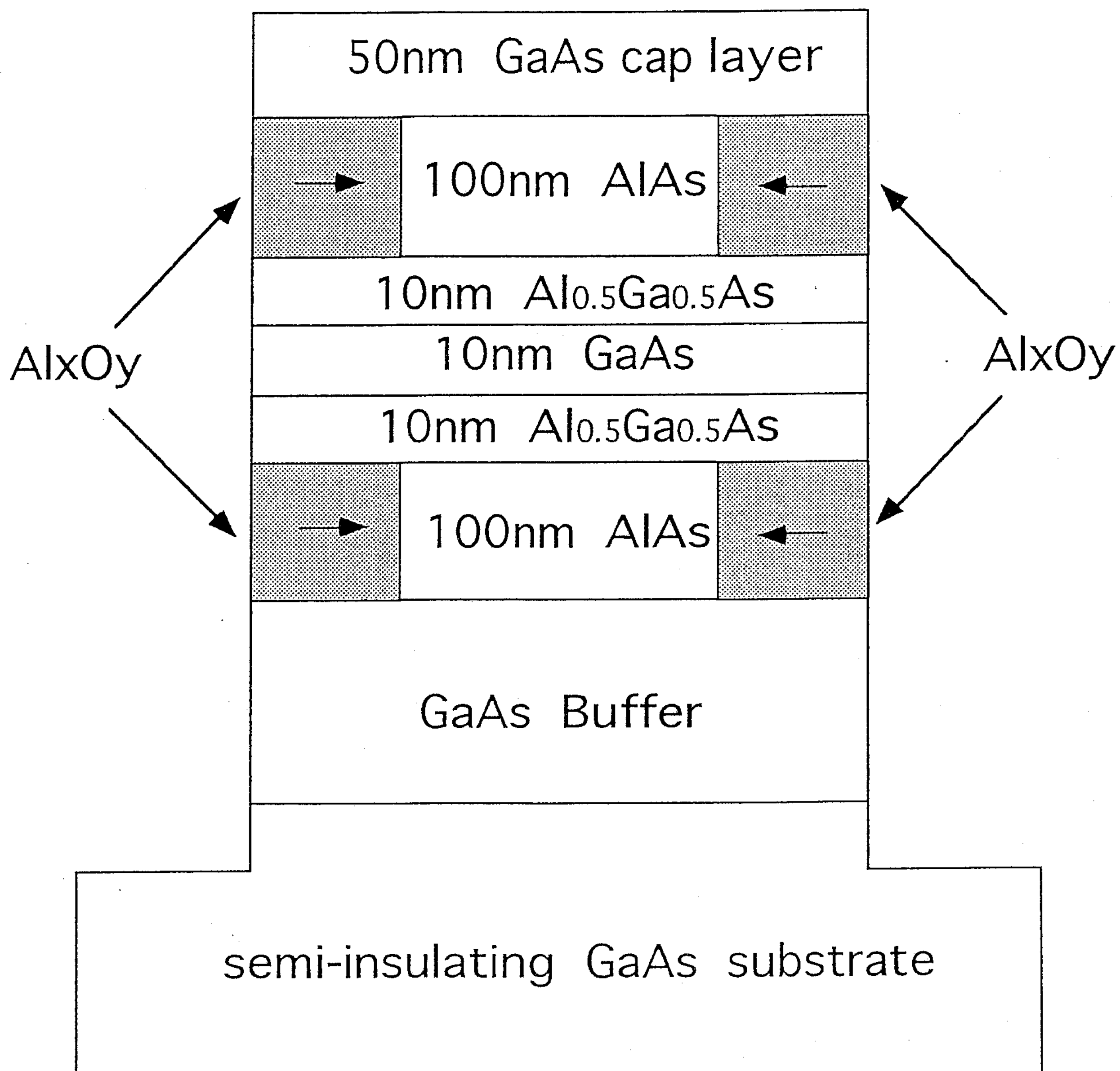

Fig. 3.3 (b) Schematic drawing of a sample after oxidation (ex. structure A).

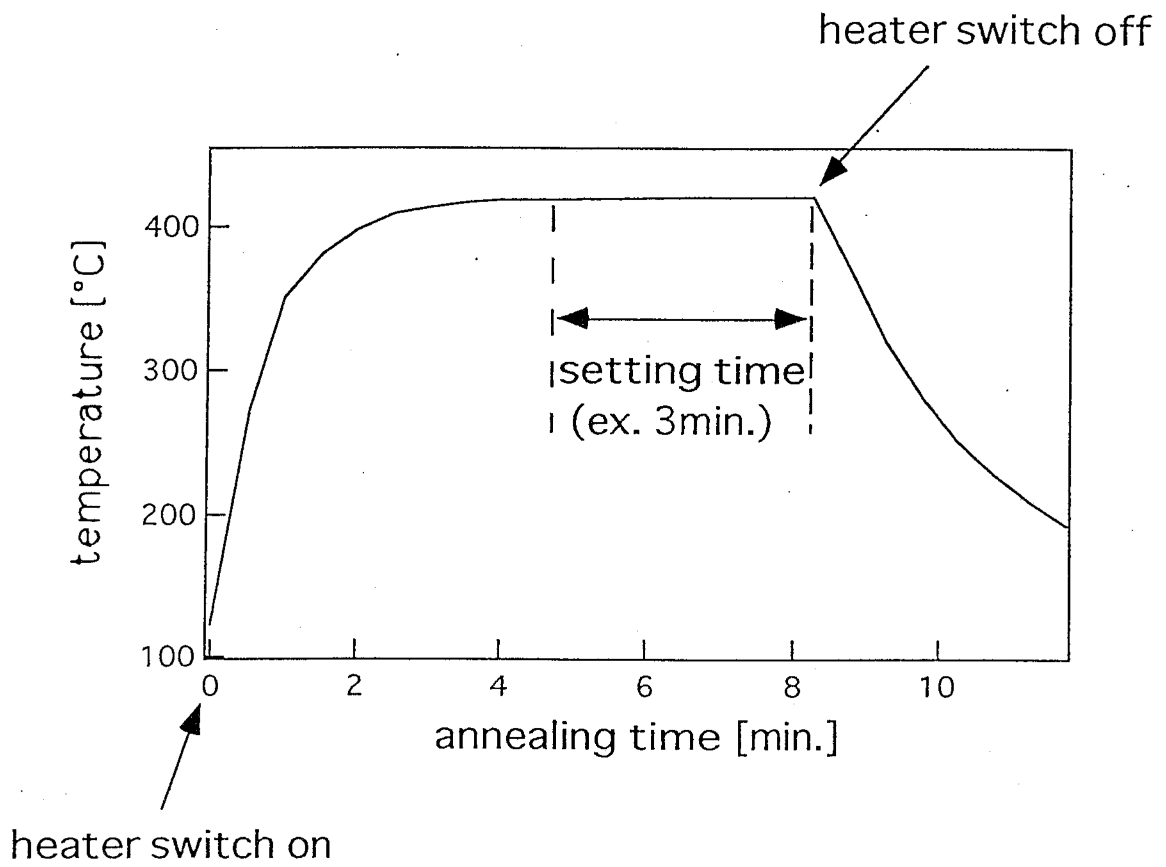

Fig. 3.4 Annealing profile of the furnace.

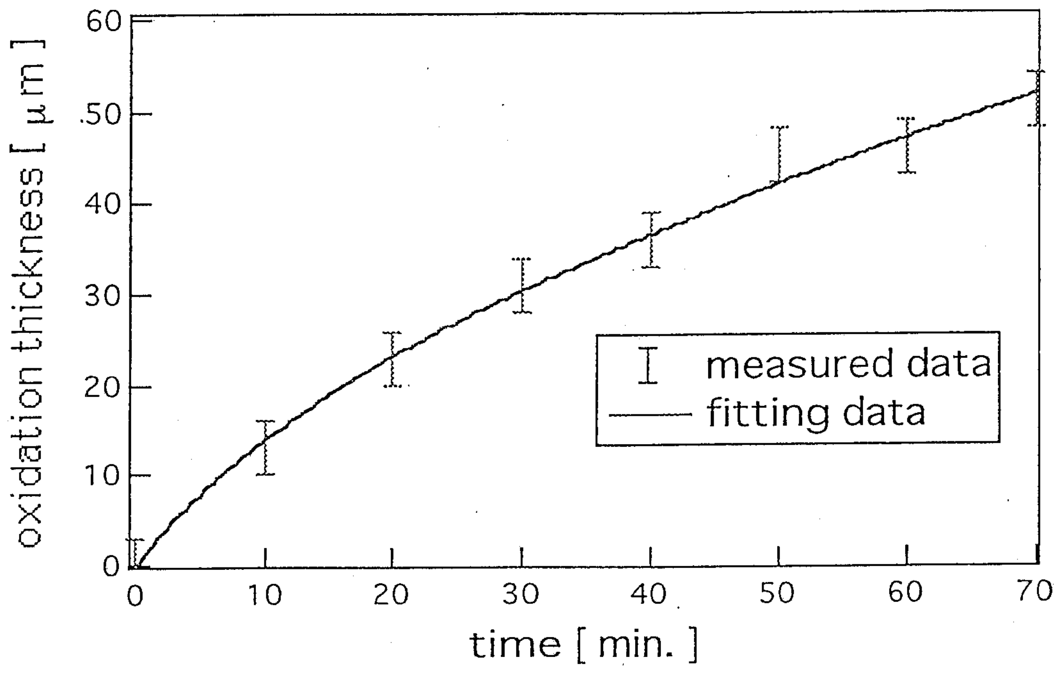

Fig. 4.1 Time dependence of the oxidation thickness (at 410 °C, oxidation direction: [110]).

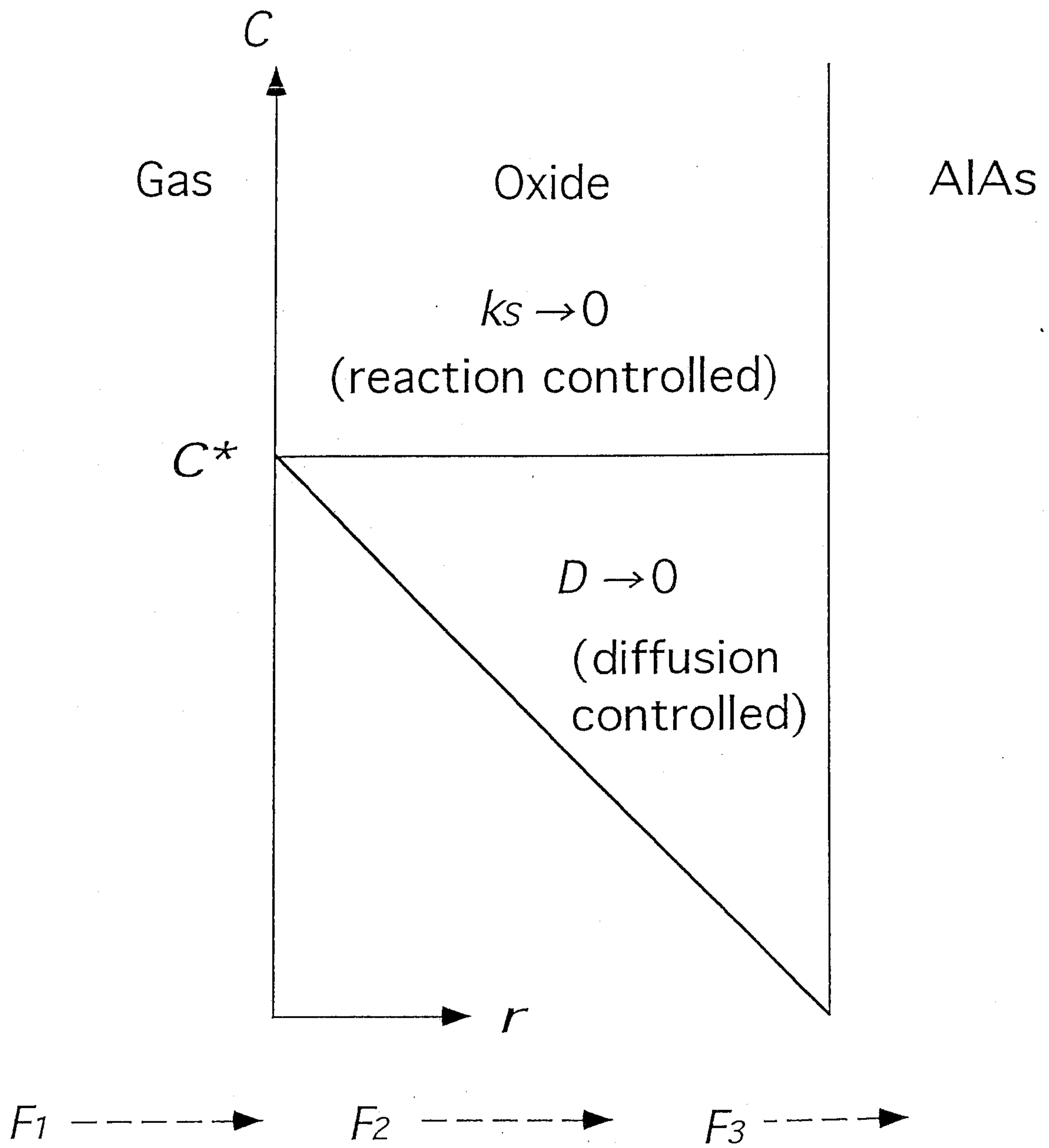

Fig. 4.2 Model for the thermal oxidation of Si or AlAs.

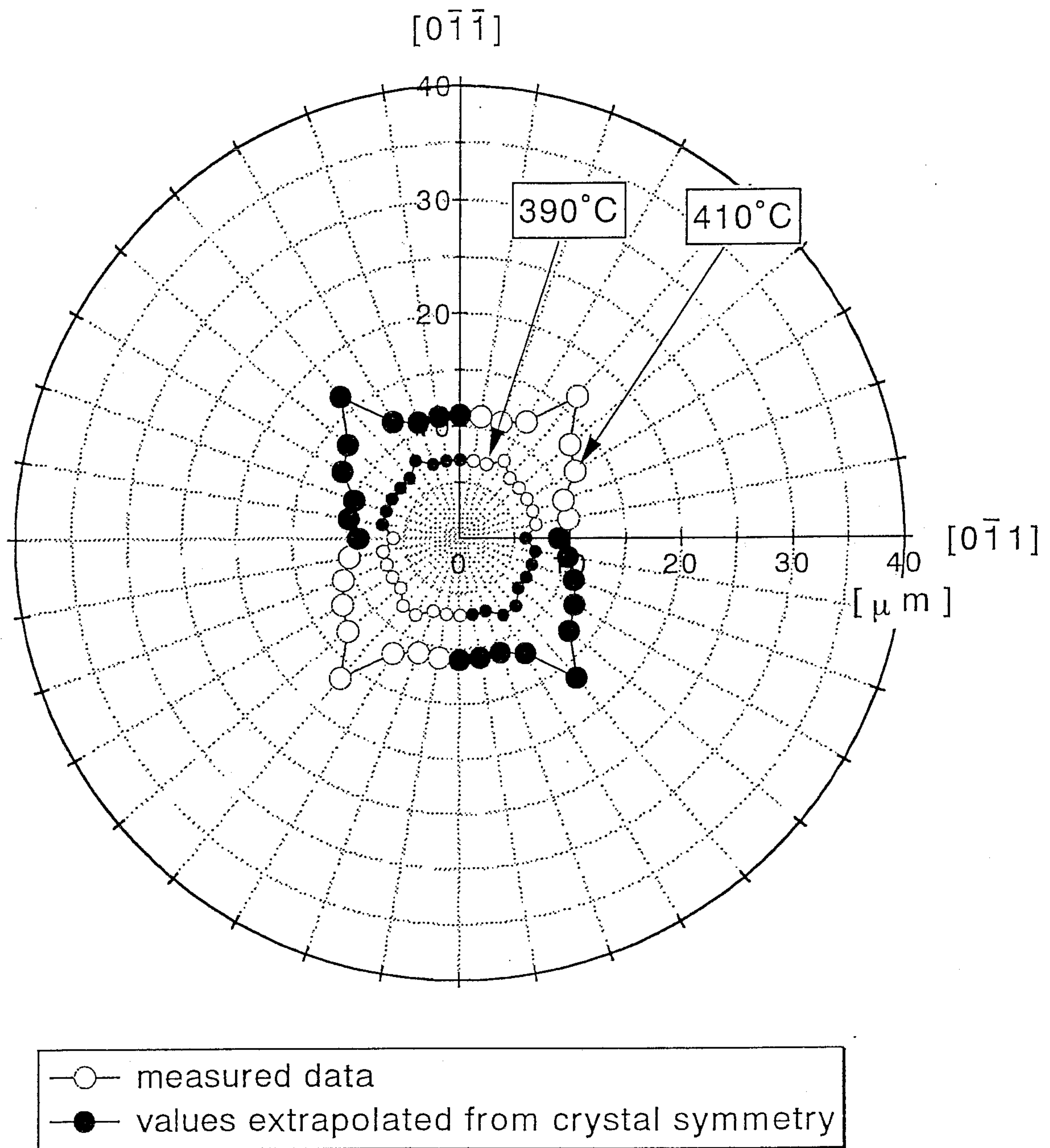

(a) (100)-oriented surface.

Fig. 4.3 Polar plot of oxidation width dependence on the direction and temperature (oxidation time: 10 min.).

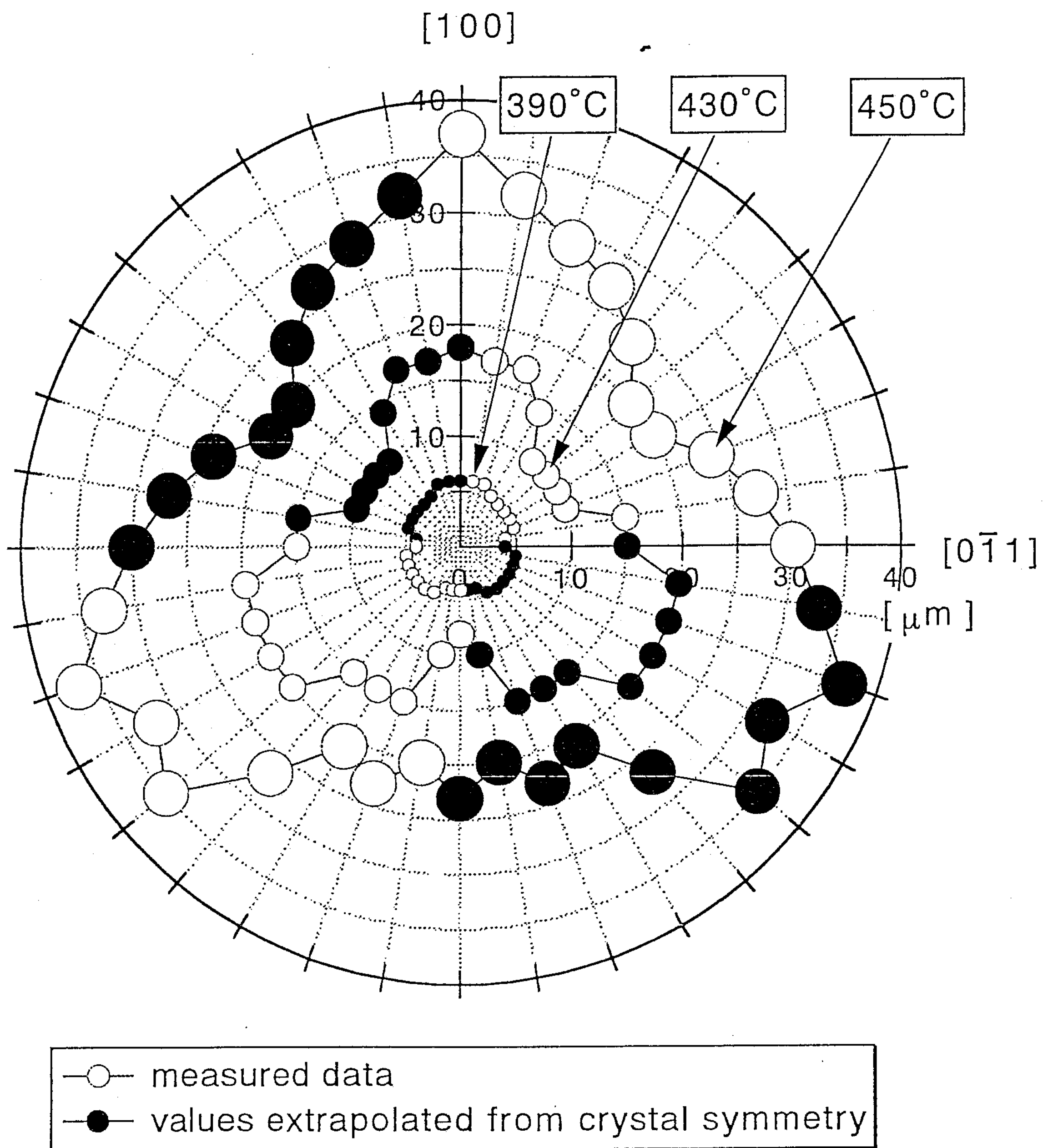

(b) (011)-oriented surface.

Fig. 4.3 Polar plot of oxidation width dependence on the direction and temperature (oxidation time: 10 min.).

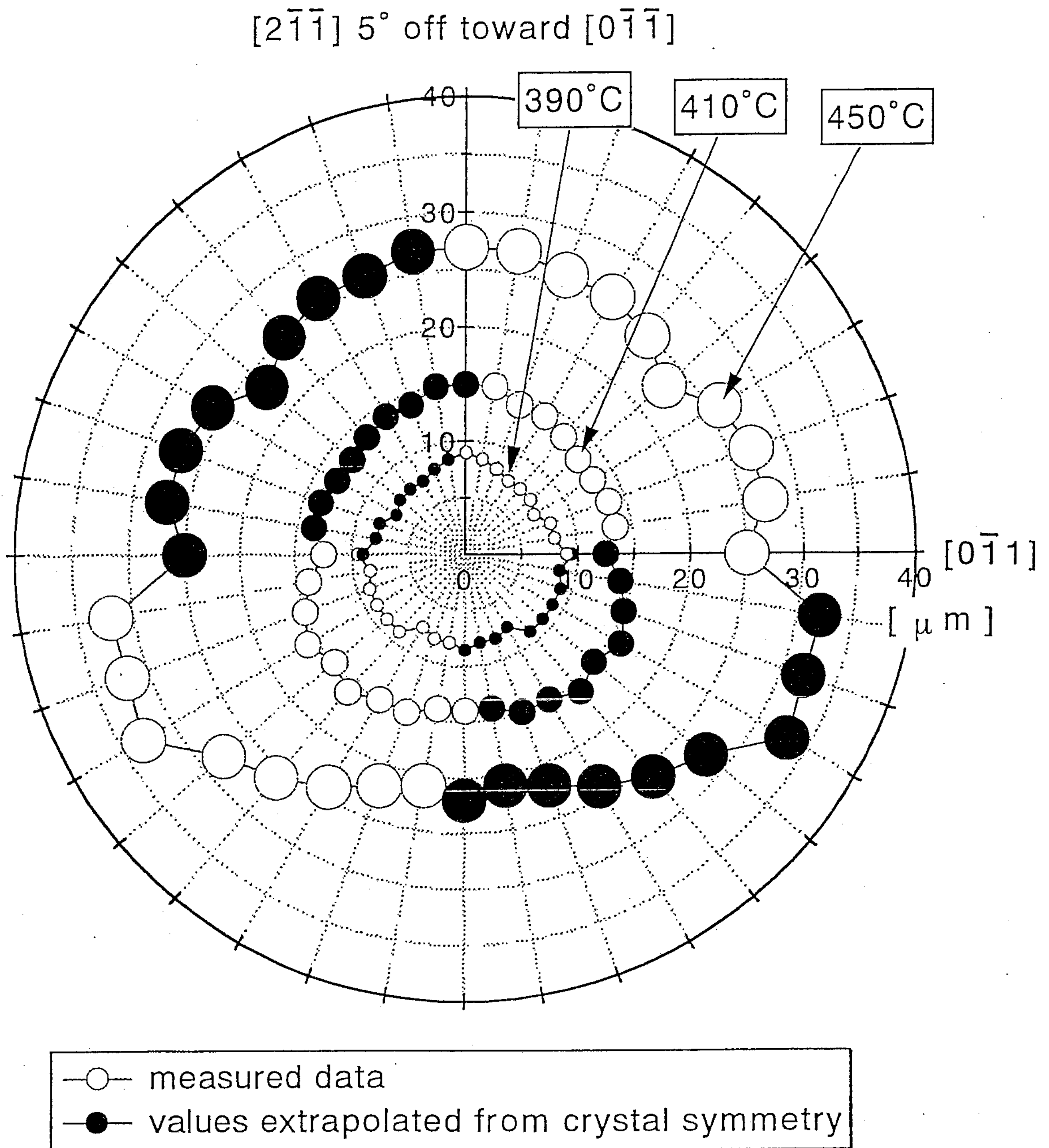

(c) (111)A 5° off toward [100]-oriented surface.

Fig. 4.3 Polar plot of oxidation width dependence on the direction and temperature (oxidation time: 10 min.).

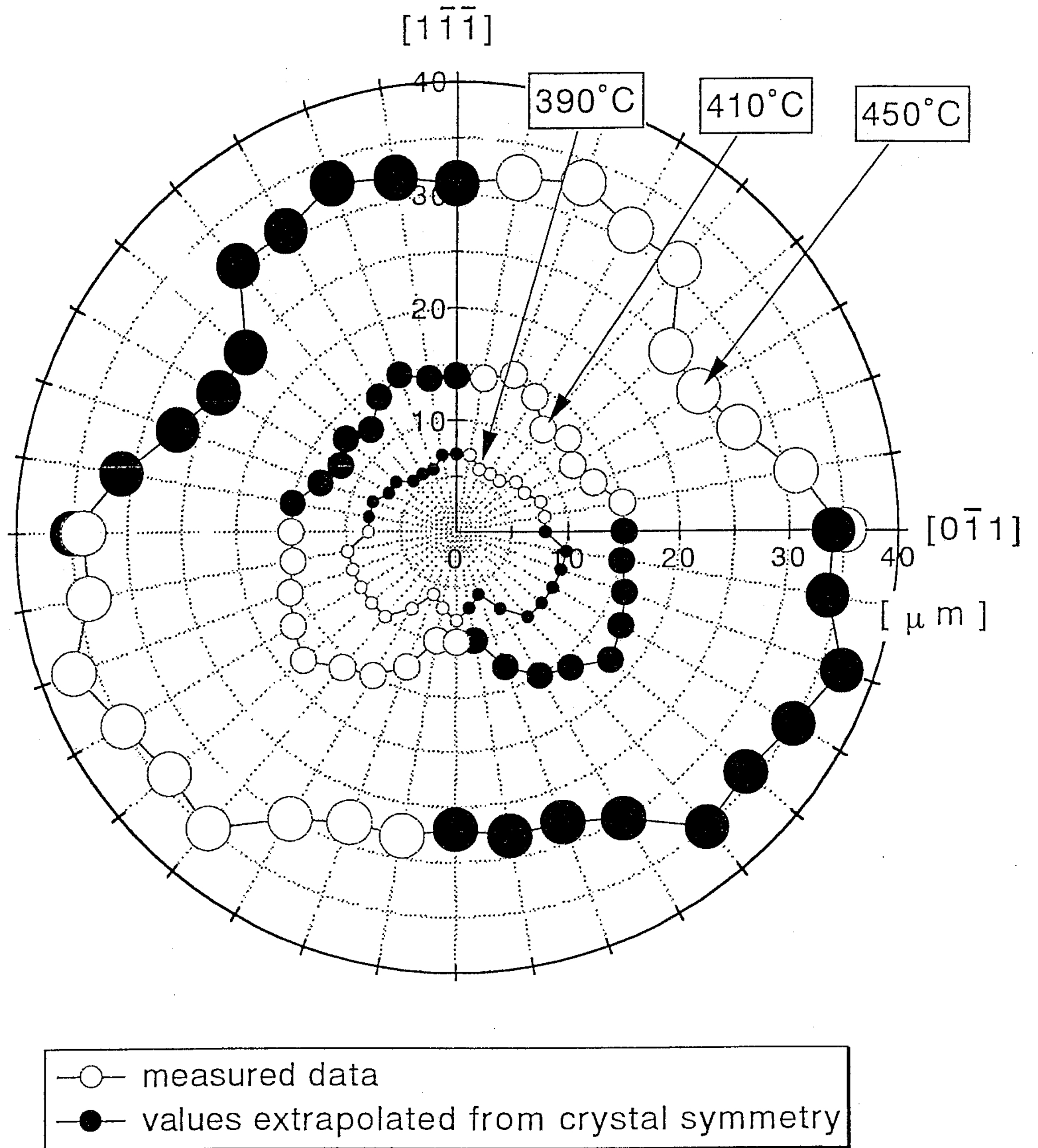

(d) (211)A-oriented surface.

Fig. 4.3 Polar plot of oxidation width dependence on the direction and temperature (oxidation time: 10 min.).

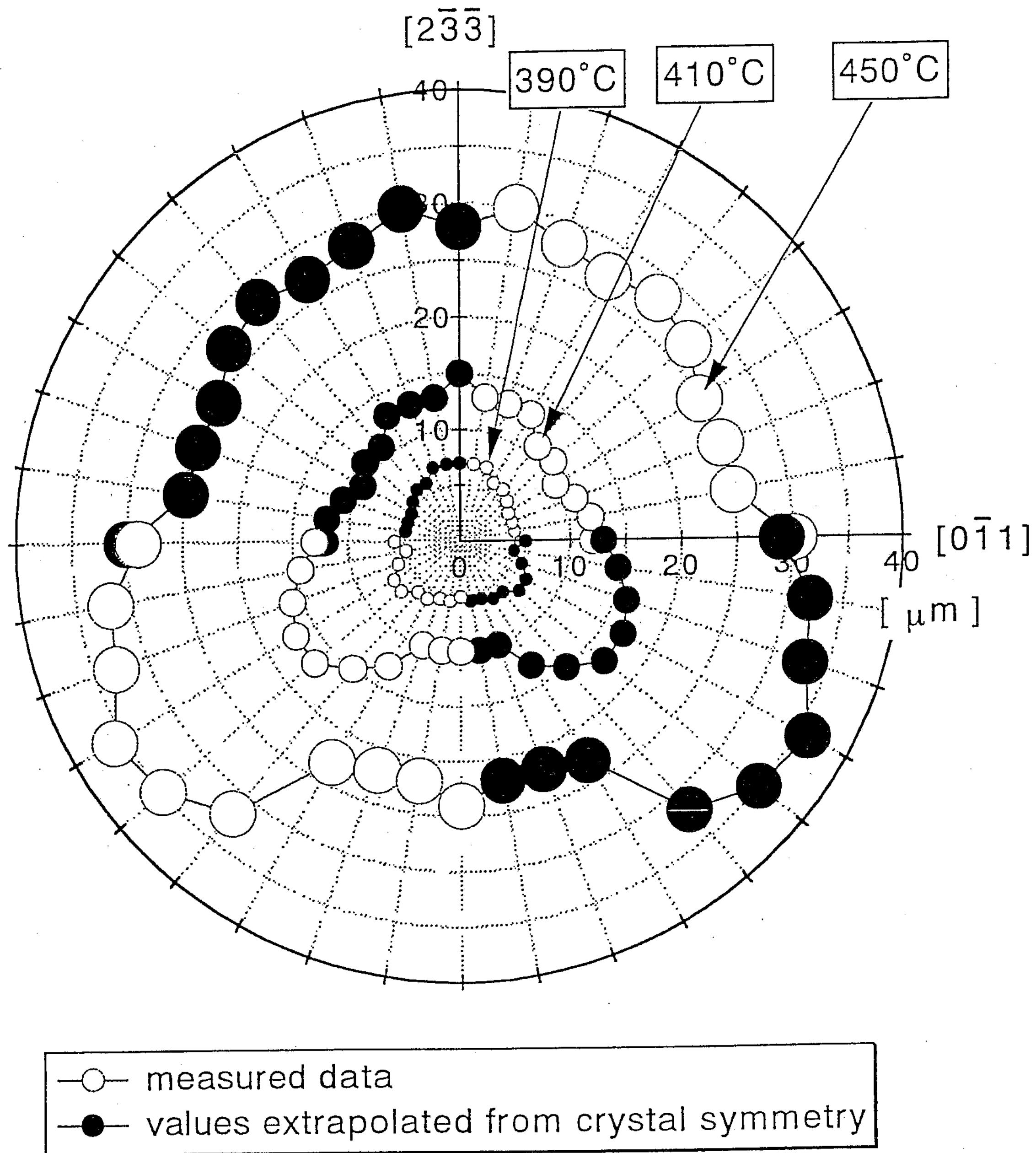

(e) (311)A-oriented surface.

Fig. 4.3 Polar plot of oxidation width dependence on the direction and temperature (oxidation time: 10 min.).

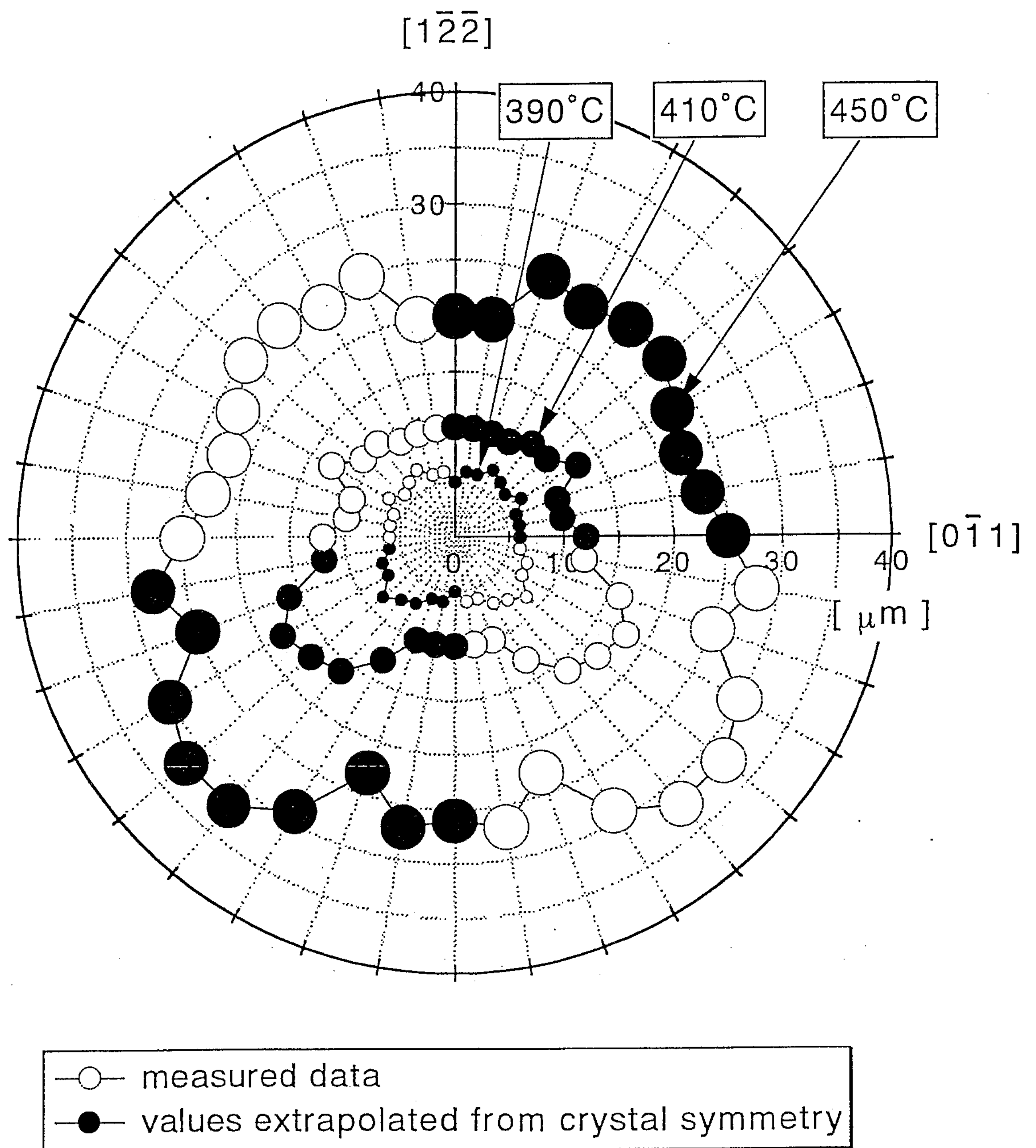

(f) (411)A-oriented surface.

Fig. 4.3 Polar plot of oxidation width dependence on the direction and temperature (oxidation time: 10 min.).

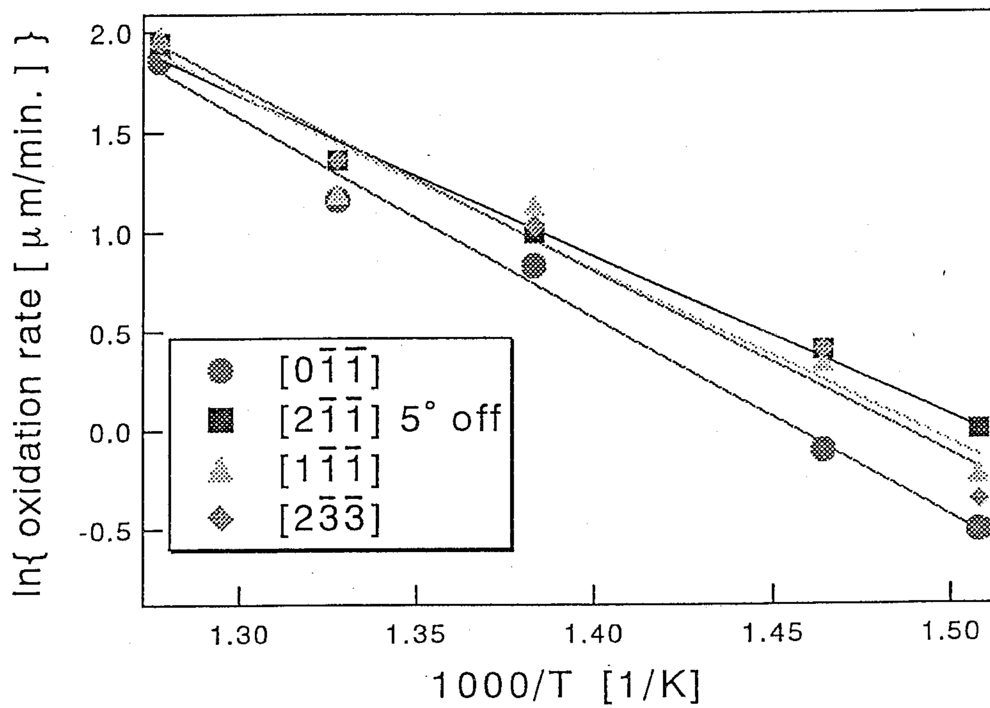

Fig. 4.5 Arrhenious plot of the oxidation rate as a function of the inverse temperature for each direction.

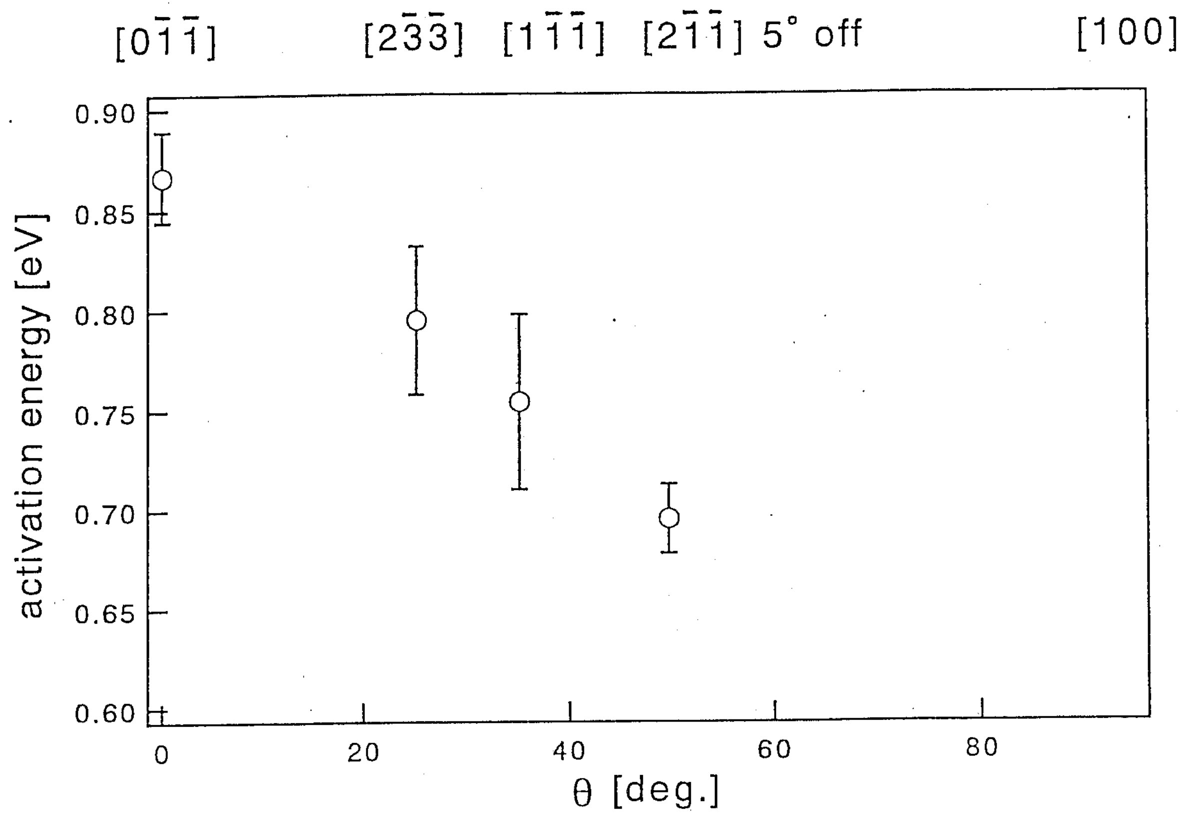

Fig. 4.6 Activation energy on the oxidation proceeding along the direction toward the [011] azimuth.

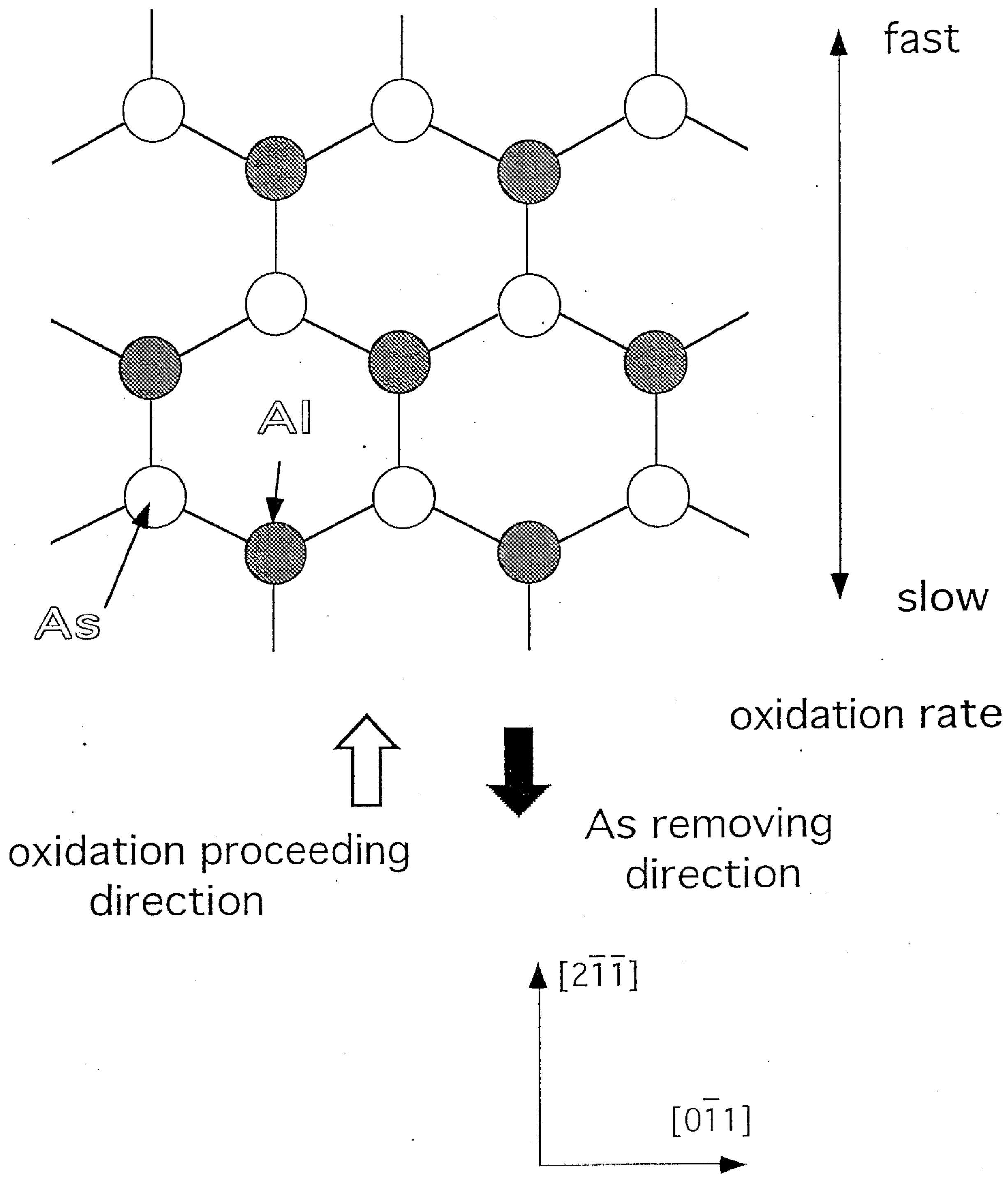

Fig. 4.7 Schematic drawing of a zinc blende structure seen from (111)A just-oriented.

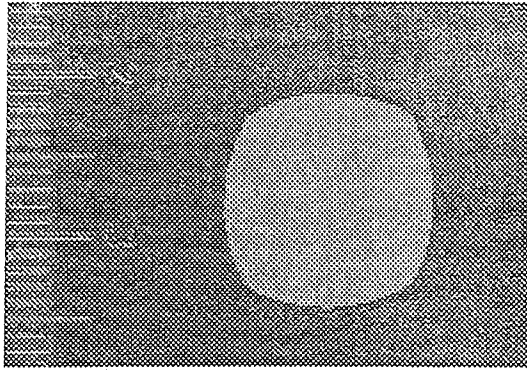

10 μm

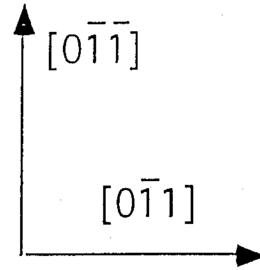

(a) (100) surface.

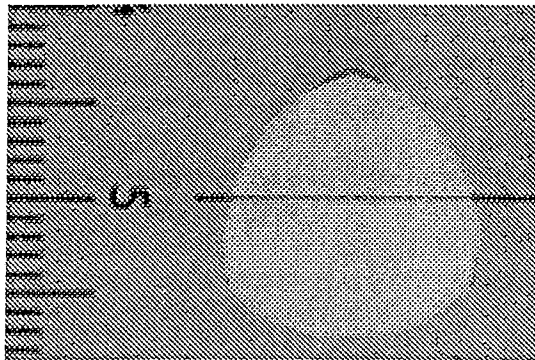

20 μm

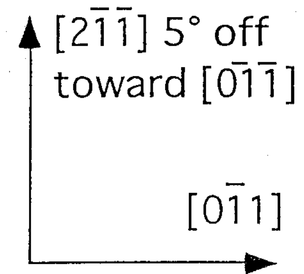

(b) (111)A5° off surface.

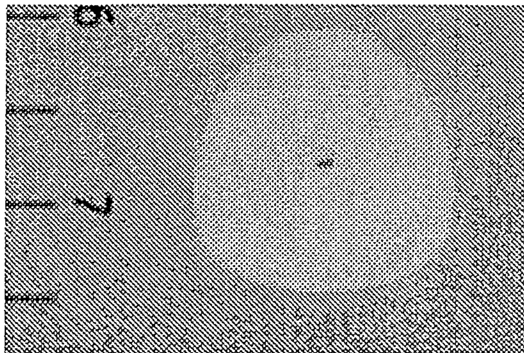

20 μm

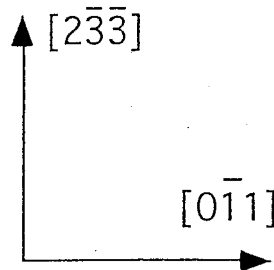

(c) (311)A surface.

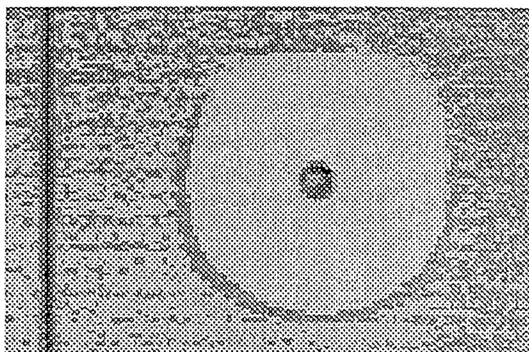

20 μm

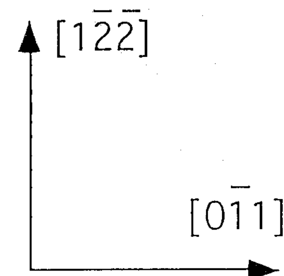

(d) (411)A surface.

Fig. 4.4 Top views of surfaces oxidized at 480℃ in samples Ⅲ with an optical microscope.

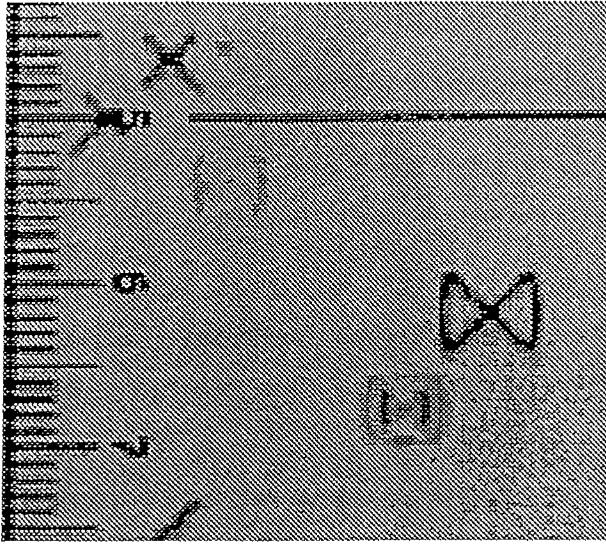

5 μm

(a) Oxidized at 570 ℃.

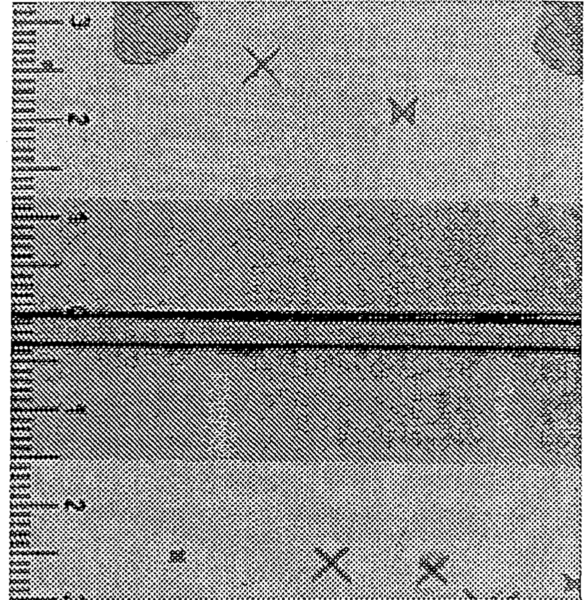

10 μm

(b) Oxidized at 570 ℃.

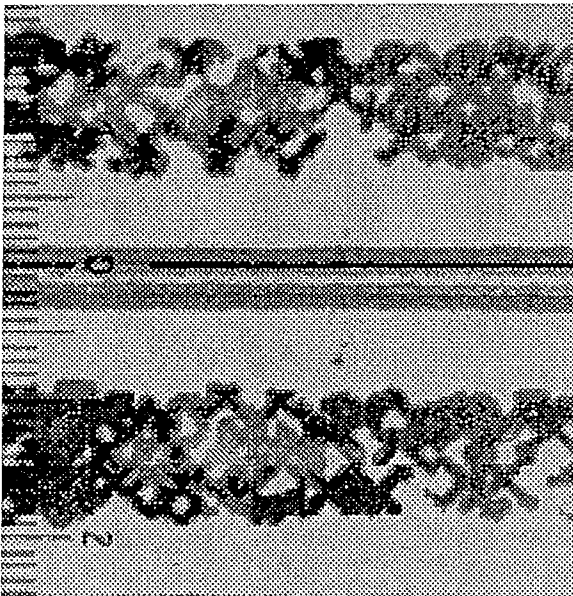

20 μm

(c) Oxidized at 600 ℃.

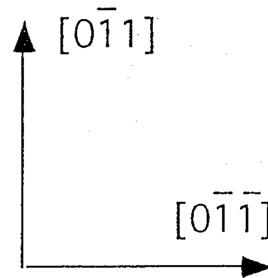

Fig. 4.8 Top views of (100) surfaces oxidized over 570 °C with an optical microscope.

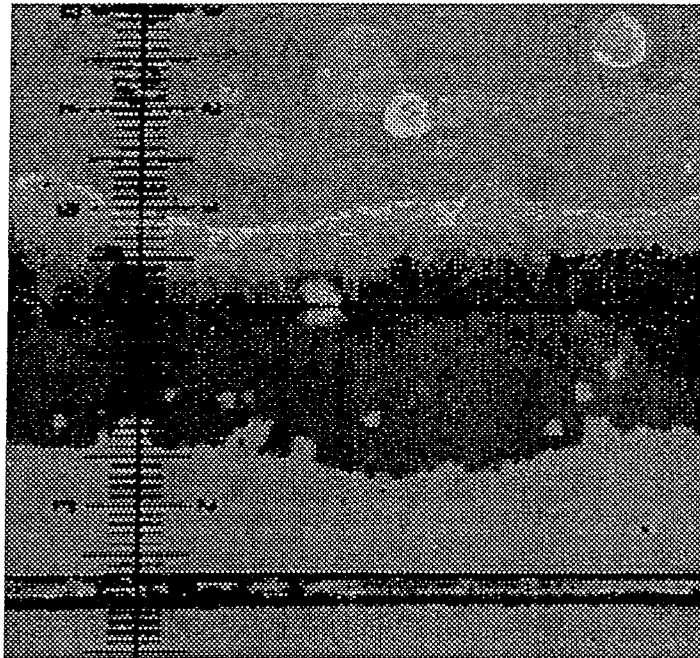

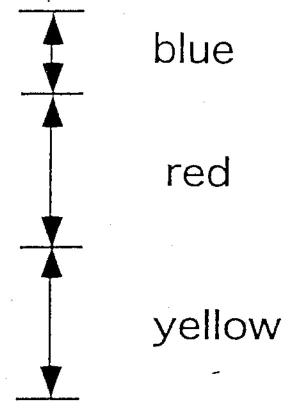

20 μm

(a) (111)A 5° off surface.

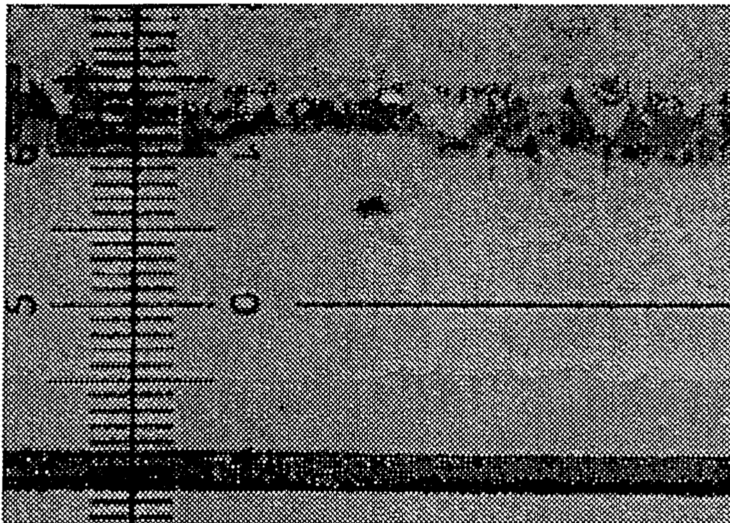

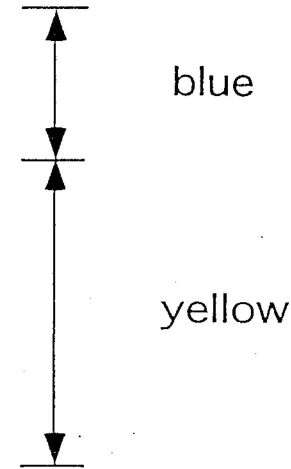

20 μm

(b) (211)A, (311)A, and (411)A surfaces.

Fig. 4.9 Top views of (n11)A surfaces oxidized at 600 °C with an optical microscope.

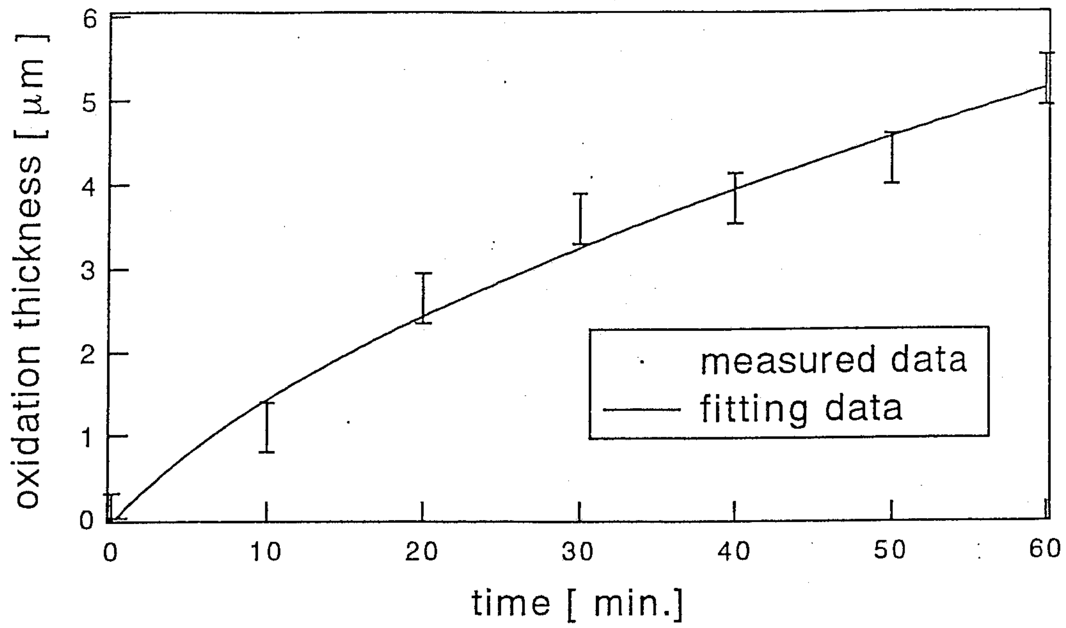

(a) Continuos oxidation.

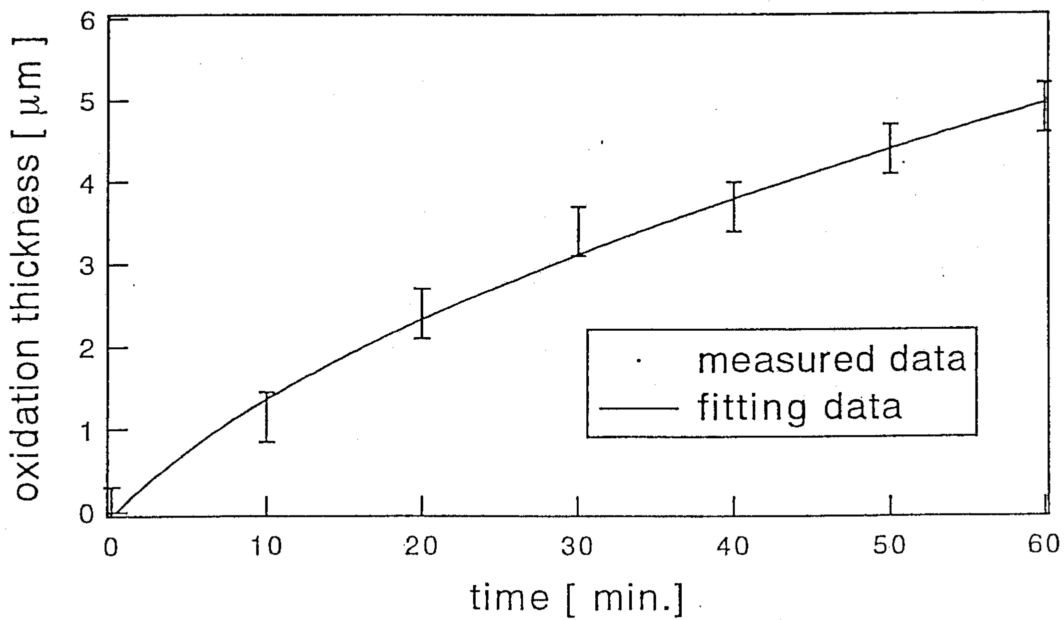

(b) Addtional oxidation.

Fig. 4.10 Time dependence of the oxidation thickness (at 380°C).

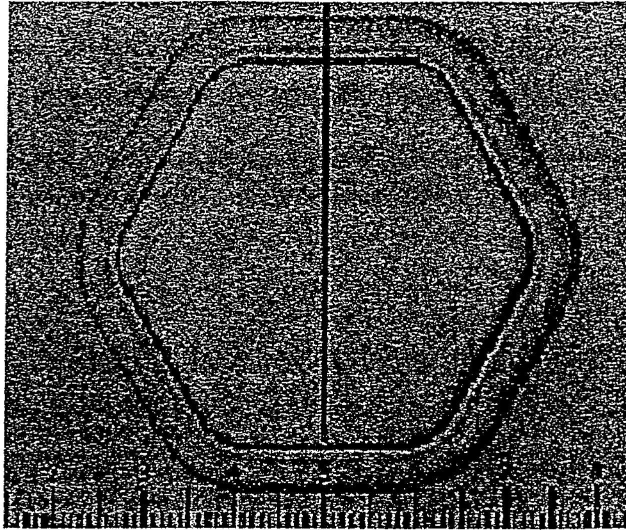

10 µm

(a) Continuous oxidized.

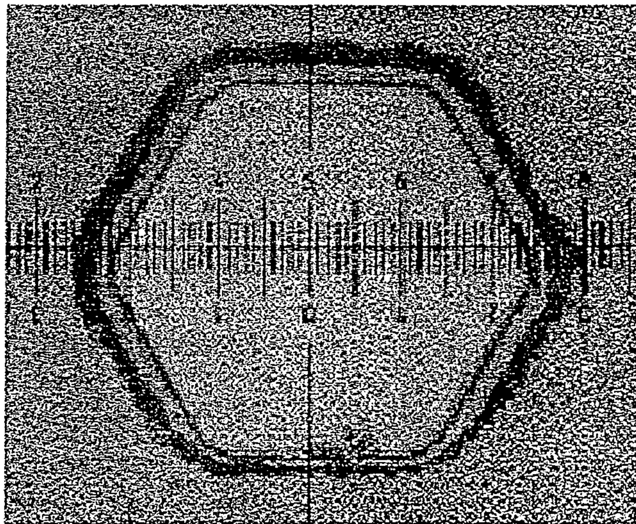

10 µm

(b) Additional oxidized.

Fig. 4.11 Top views of (311)A surfaces oxidized at 380 °C with an optical microscope.

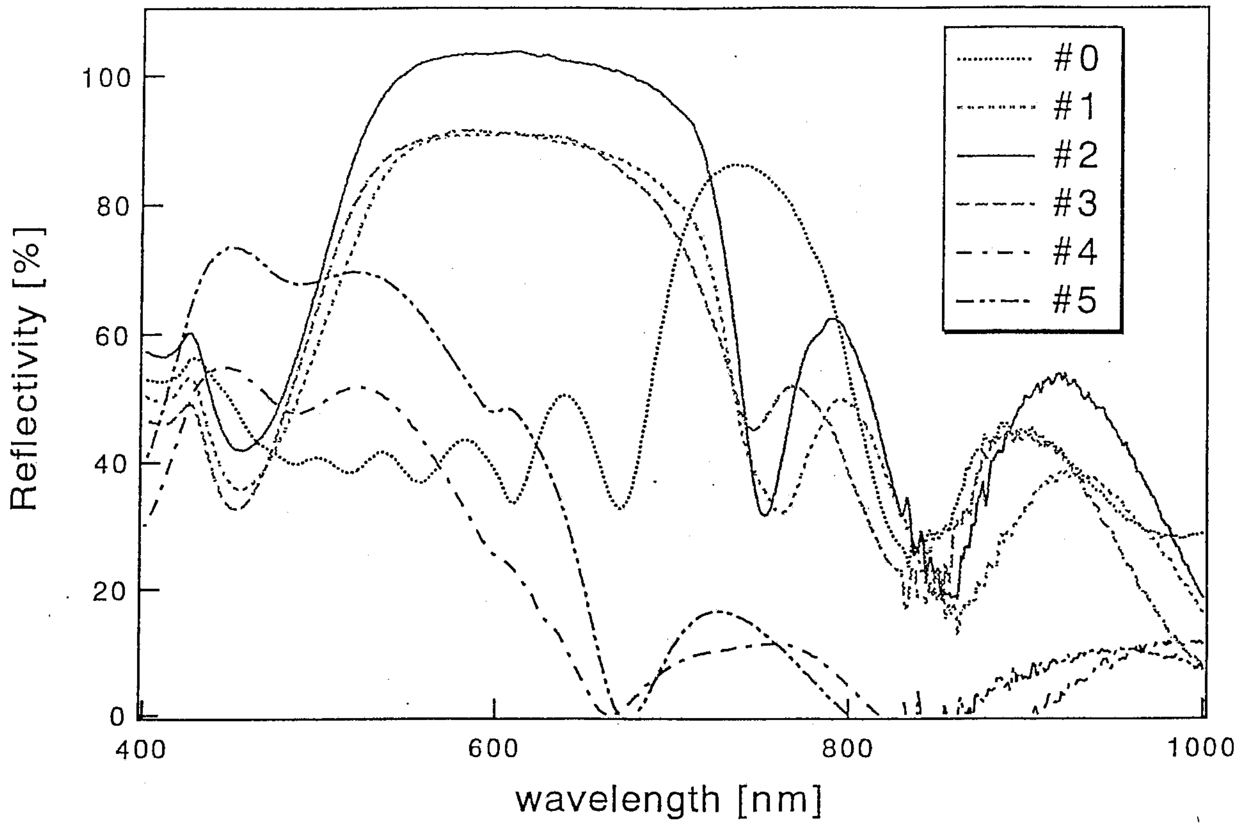

(a) (100)-oriented surface.

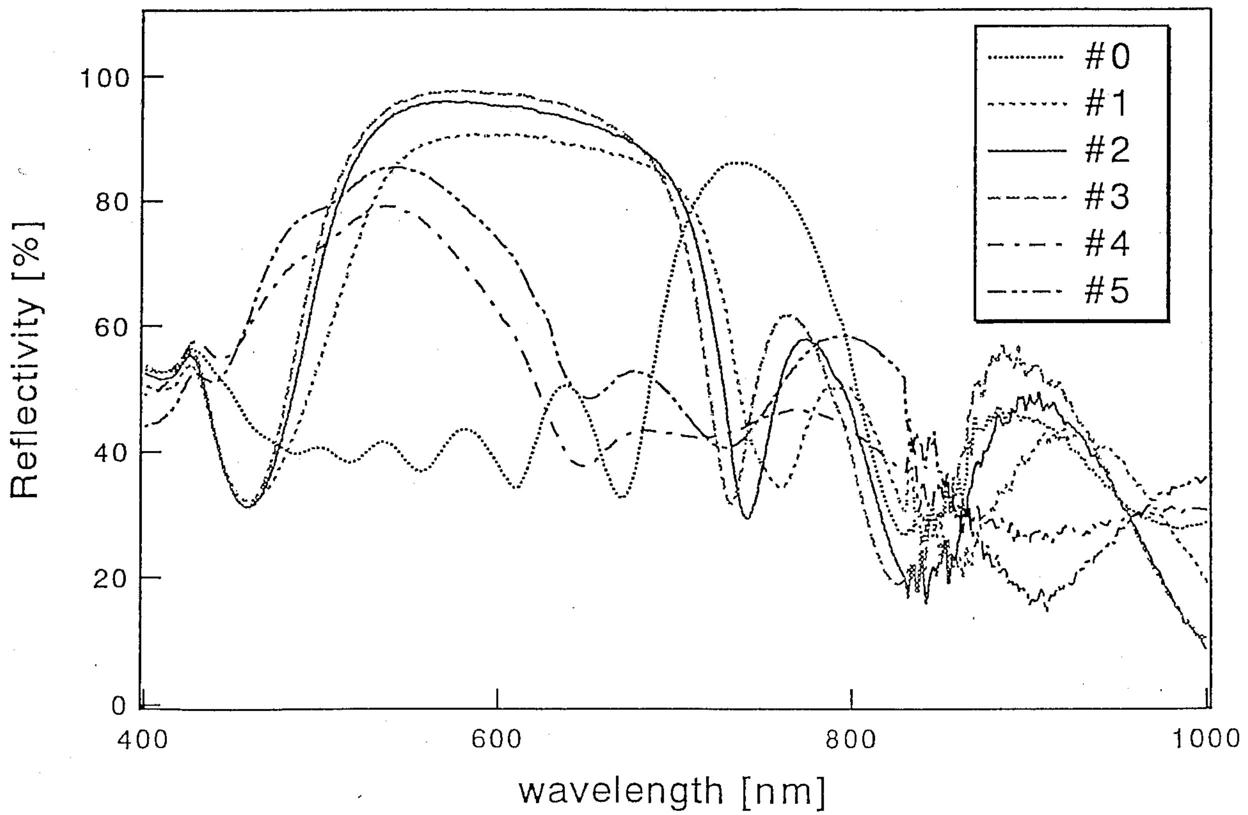

(b) (111)A 5° off-oriented surface.

Fig. 5.1 Reflectance spectra for 5-periods DBR structure.

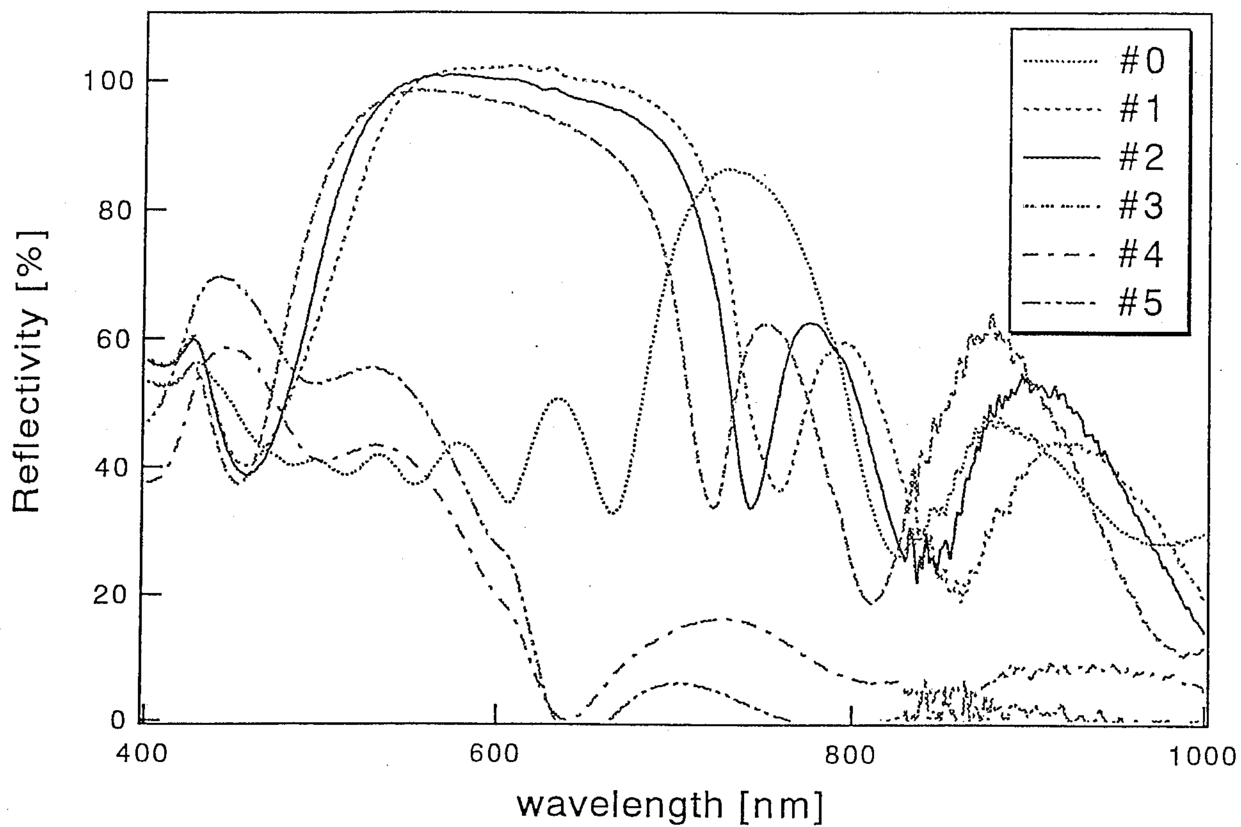

(c) (211)A-oriented surface.

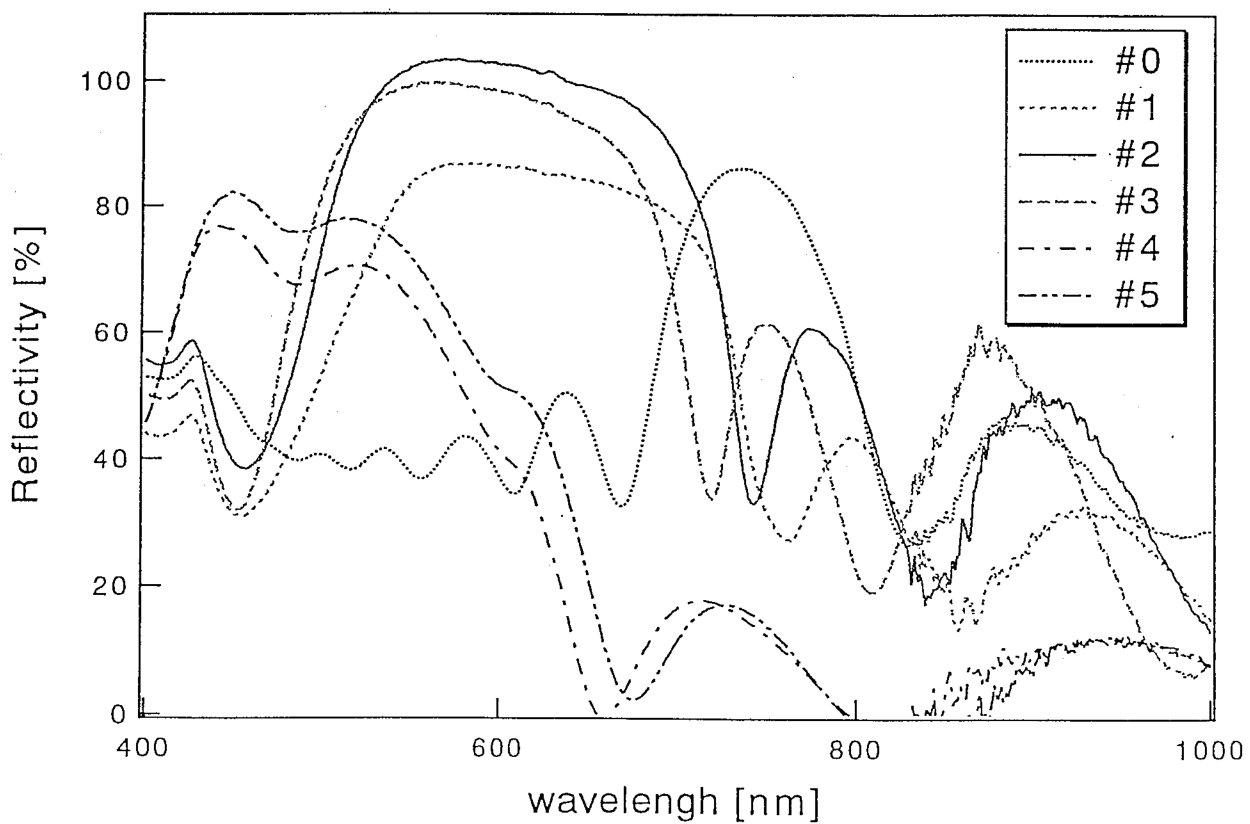

(d) (311)A-oriented surface.

Fig. 5.1 Reflectance spectra for 5-periods DBR structure.

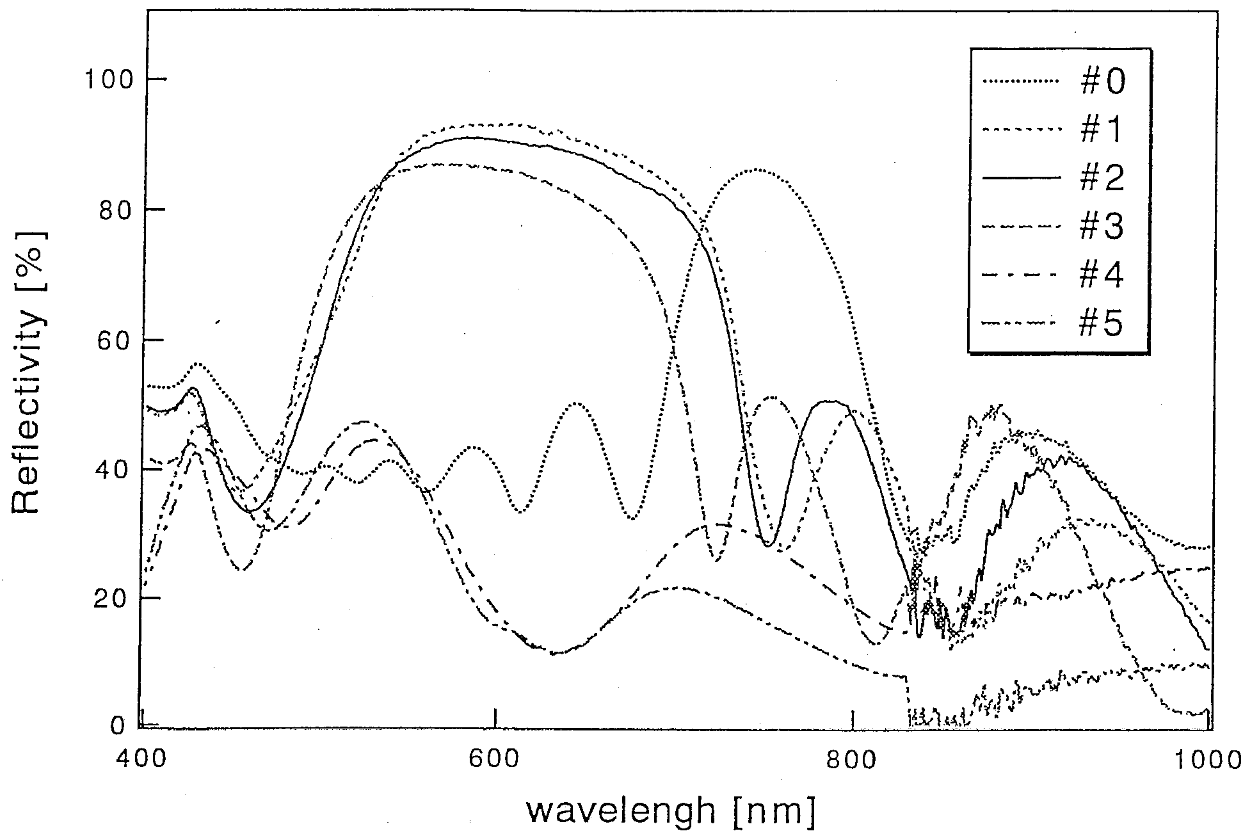

(e) (411)A-oriented surface.

Fig. 5.1 Reflectance spectra for 5-periods DBR structure.

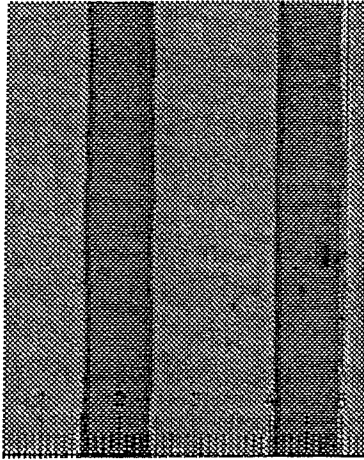

(a) Oxidized at 410 °C.

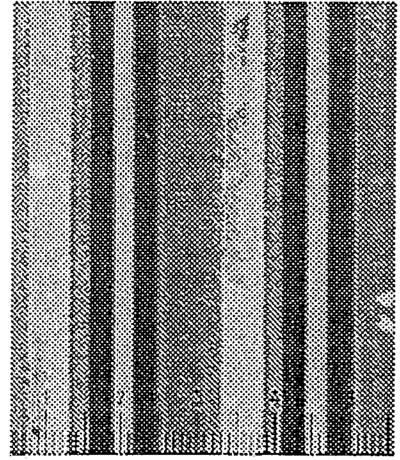

(b) Oxidized at 470 °C.

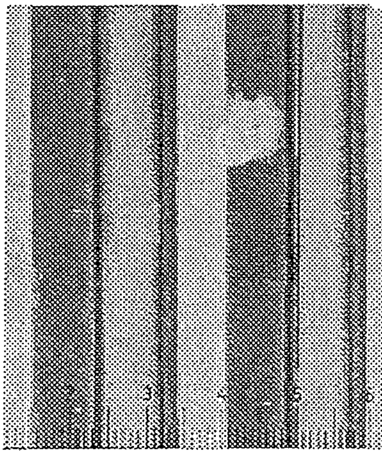

(c) Oxidized at 490 °C.

Fig. 5.2 Top views of a DBR surfaces completely oxidized with optical microscope ((411)A).

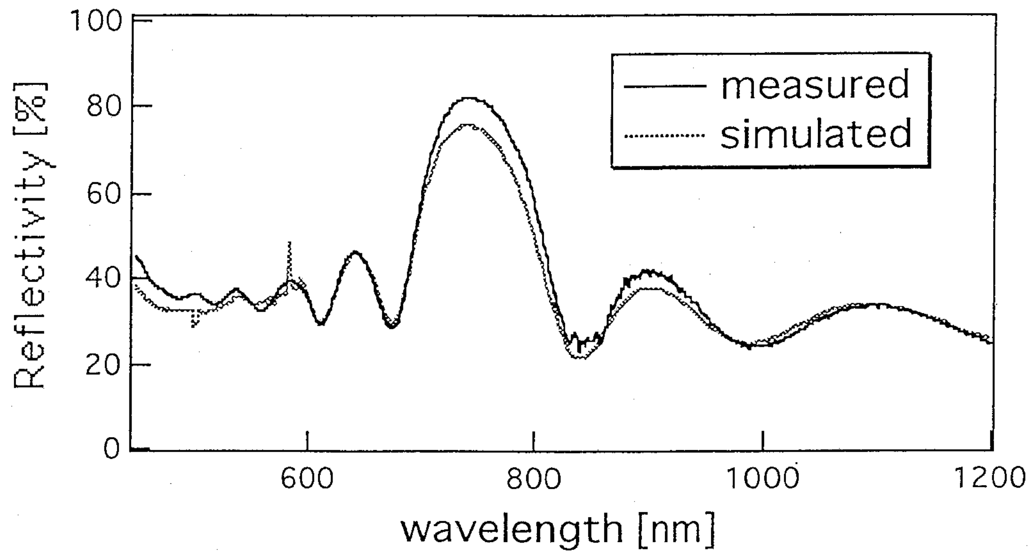

(a) before oxidation
(AlGaAs: 30 nm, AlAs: 46 nm).

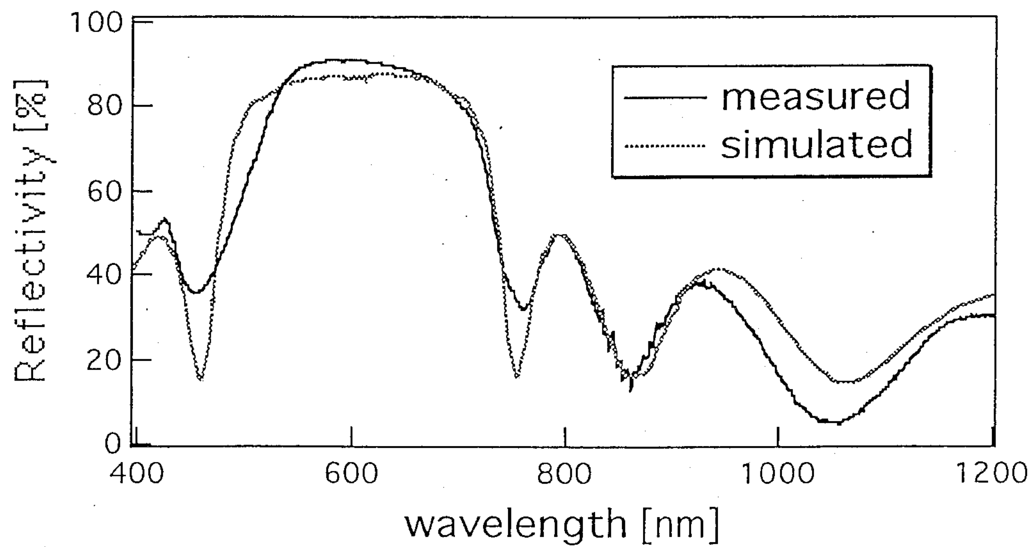

(b) oxidized at 410℃.
(AlGaAs: 29 nm, AlxOy: 40nm).

Fig. 5.3 Simulaiton results.
(sample orientaion: (411)A).

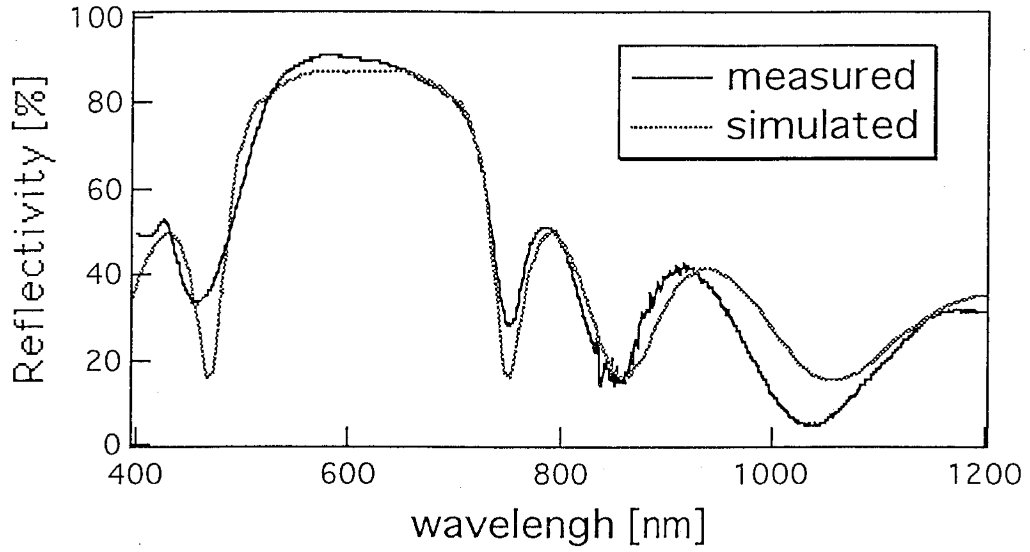

(c) oxidized at 430℃.
(AlGaAs: 29 nm, AlxOy: 37 nm).

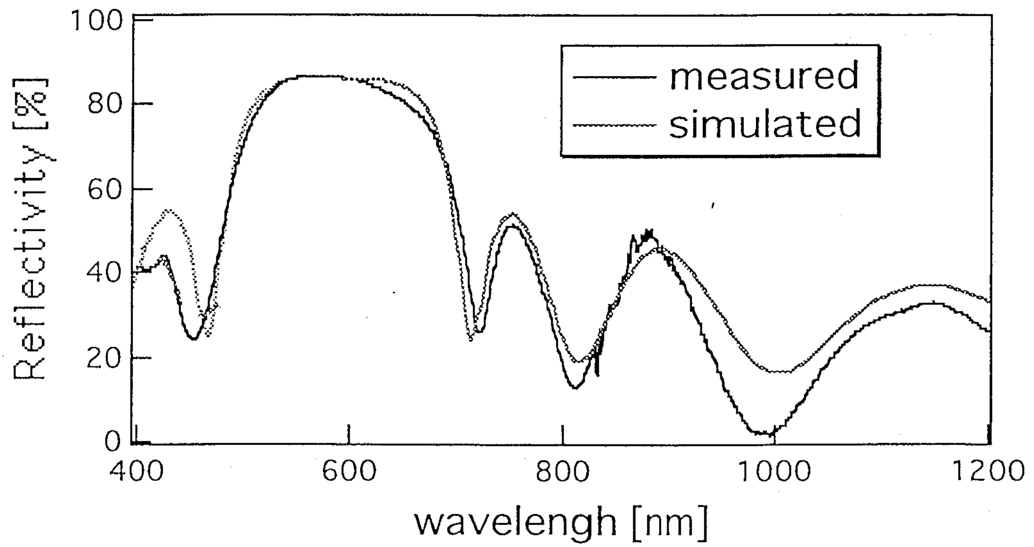

(d) oxidized at 450℃.
(AlGaAs: 29 nm, AlxOy: 31 nm).

Fig. 5.3 Simulation results.
(sample orientaion: (411)A).

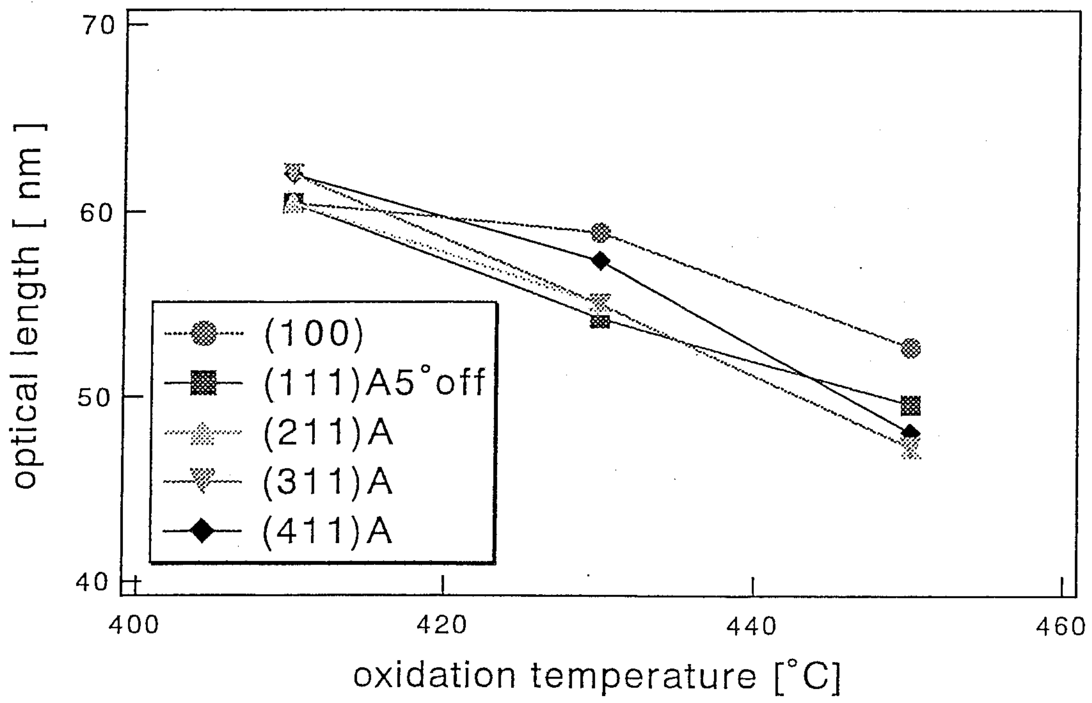

Fig. 5.4 Optical length of Al_xO_y on oxidation temperature.
optical length = n · L.

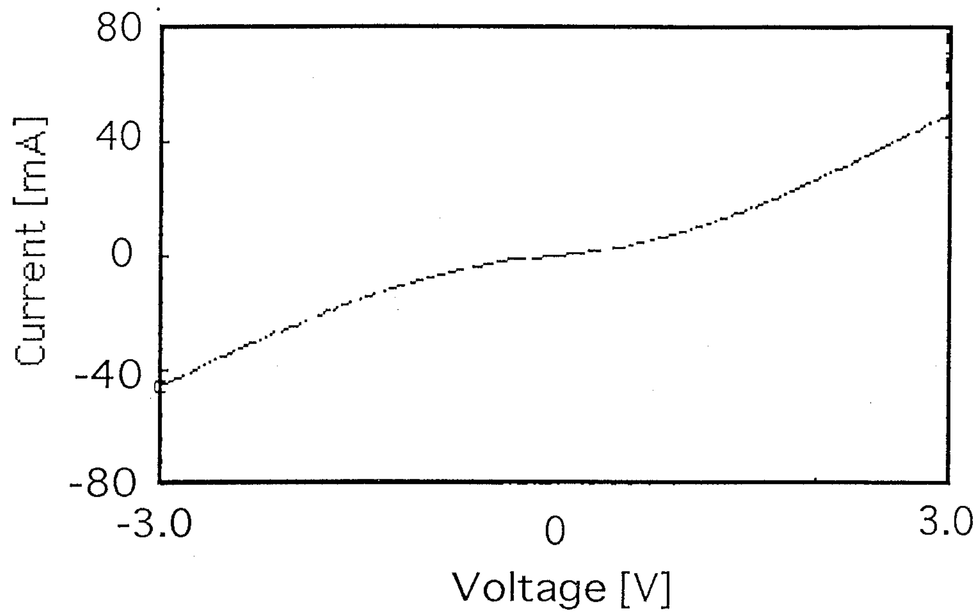

(1) Without annealing.

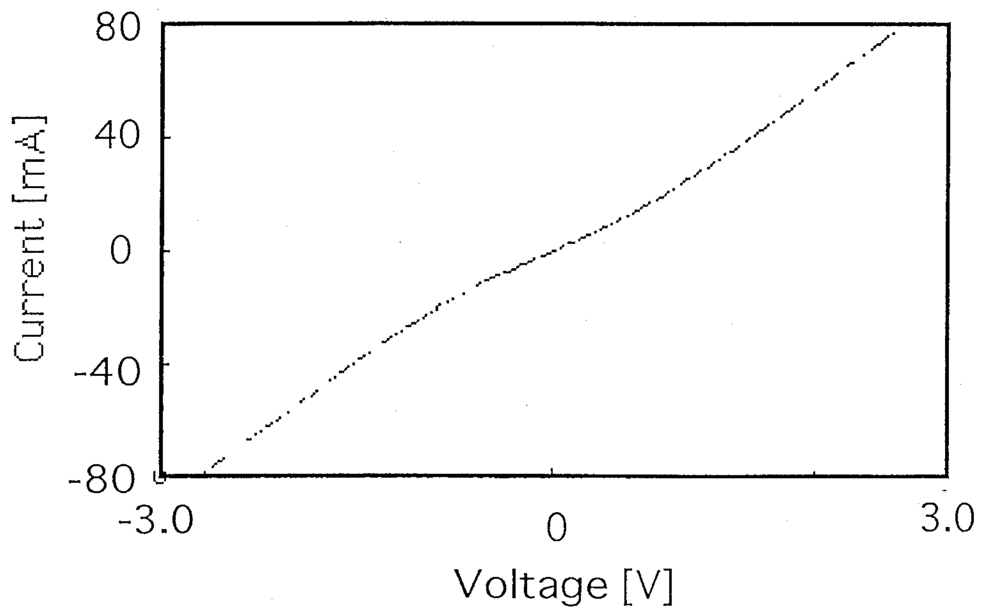

(2) Annealed at 400 °C for 1.5 min.

Fig. 6.1 (a) I-V characteristics of p-type GaAs between Mn/Au contacts (contact separation length: 10 μm).

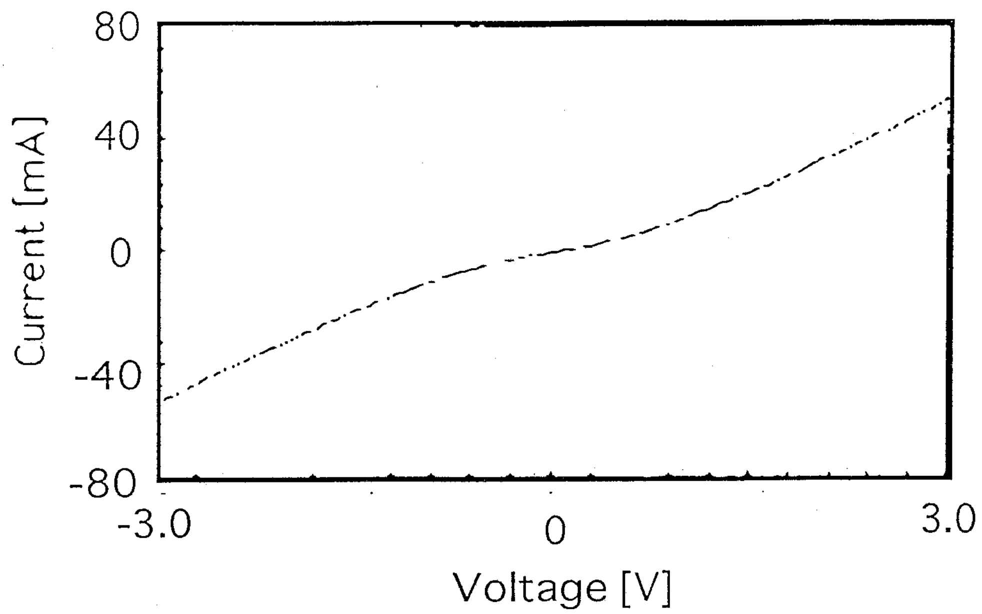

(1) Without annealing.

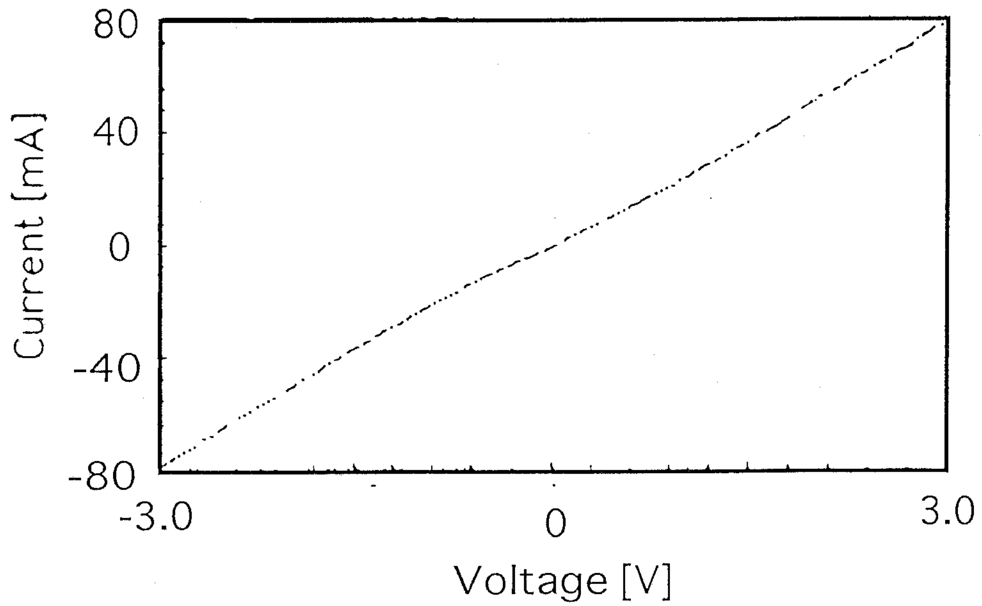

(2) Annealed at 380 °C for 1.5 min.

Fig. 6.1 (b) I-V characteristics of p-type GaAs between Mn/Au contacts (contact separation length: 20 μm).

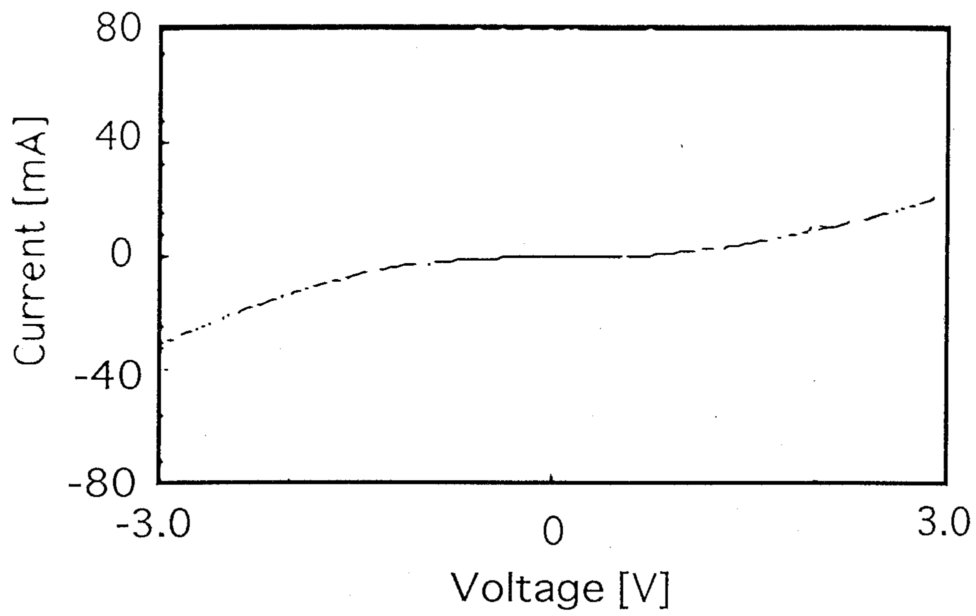

(1) Without annealing.

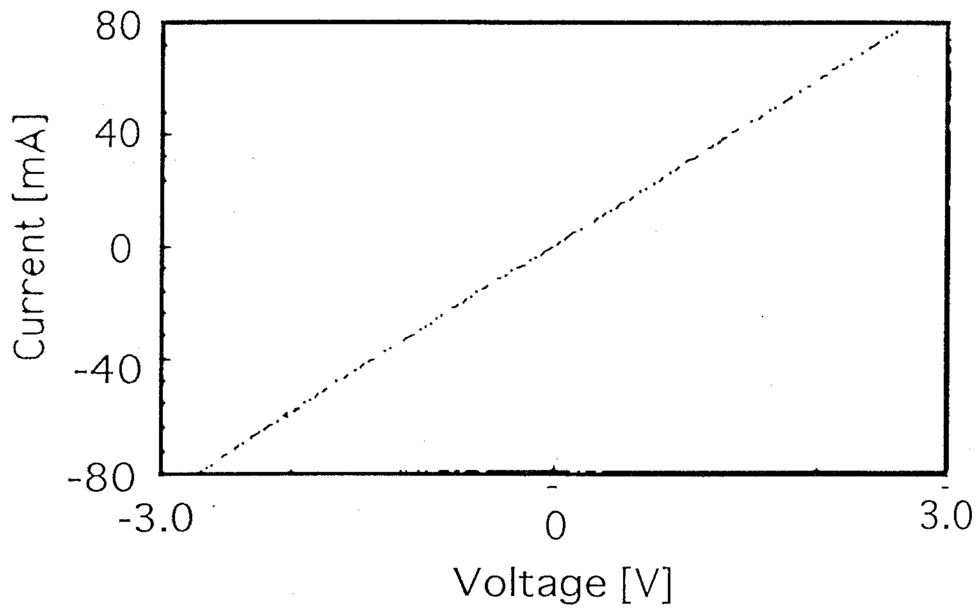

(2) Annealed at 400 °C for 1.5 min.

Fig. 6.1 (c) I-V characteristics of p-type GaAs between Mn/Au contacts (contact separation length: 20 μm).

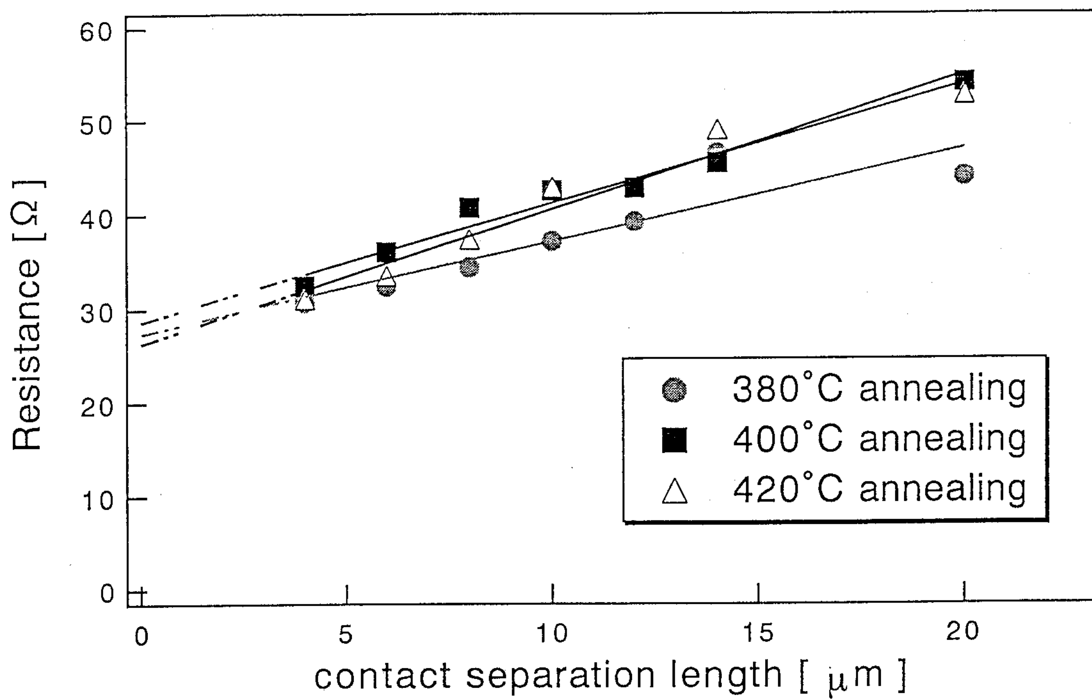

(1) Applied voltage: 1 [v].

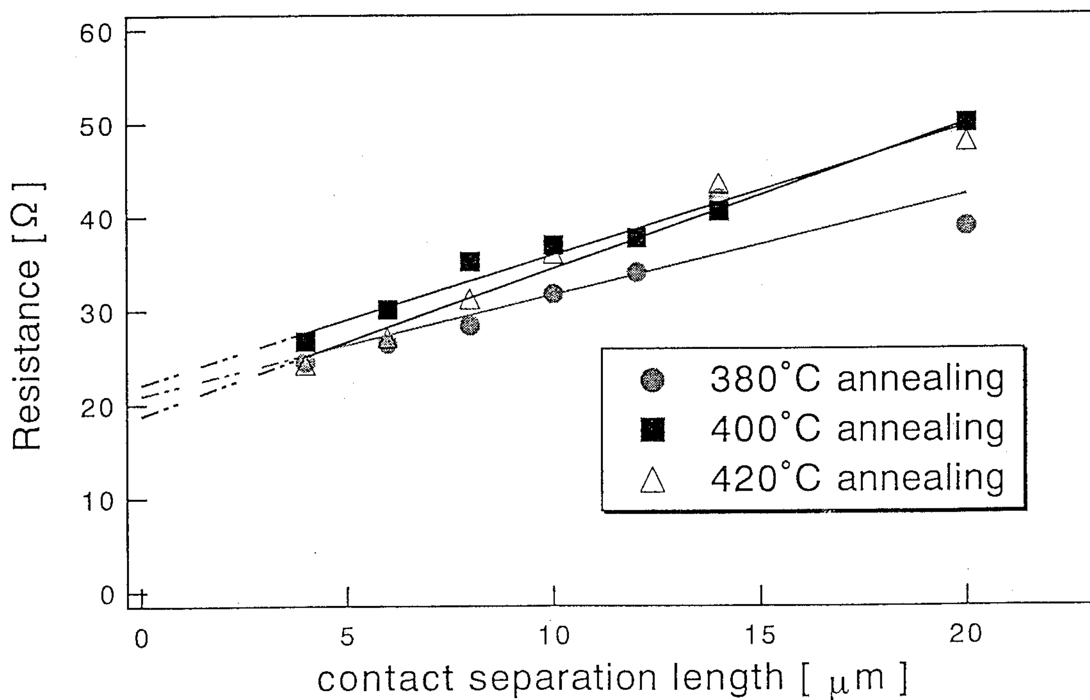

(2) Applied voltage: 2 [v].

Fig. 6.2 (a) Plot of measured resistance as a function of contact searation length (Mn/Au).

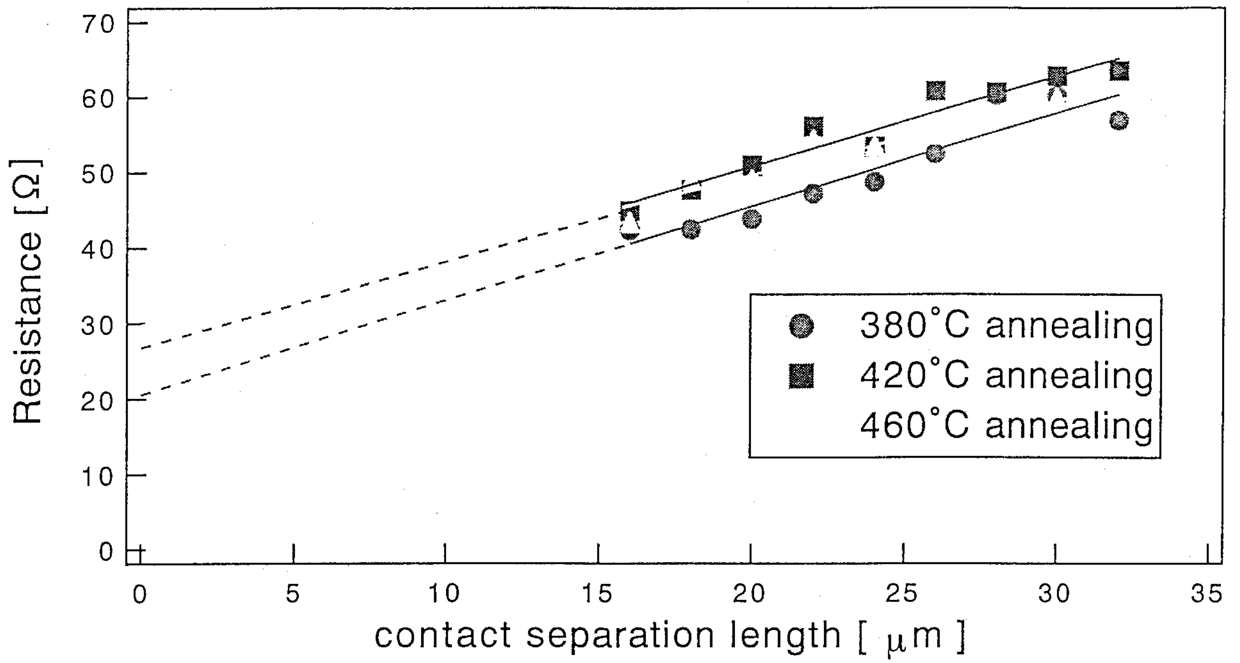

(1) Applied voltage: 1[V].

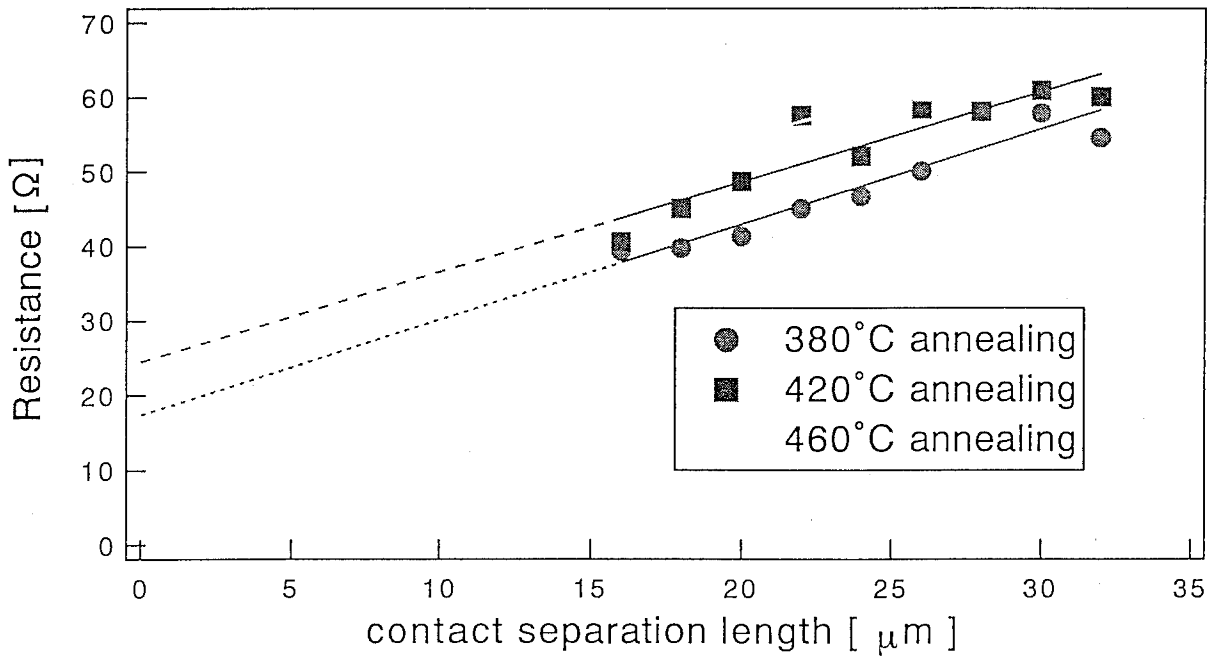

(2) Applied voltage: 2[V].

Fig. 6.2 (b) Plot of measured resistance as a function of contact separation length (Ti/Pt/Au).

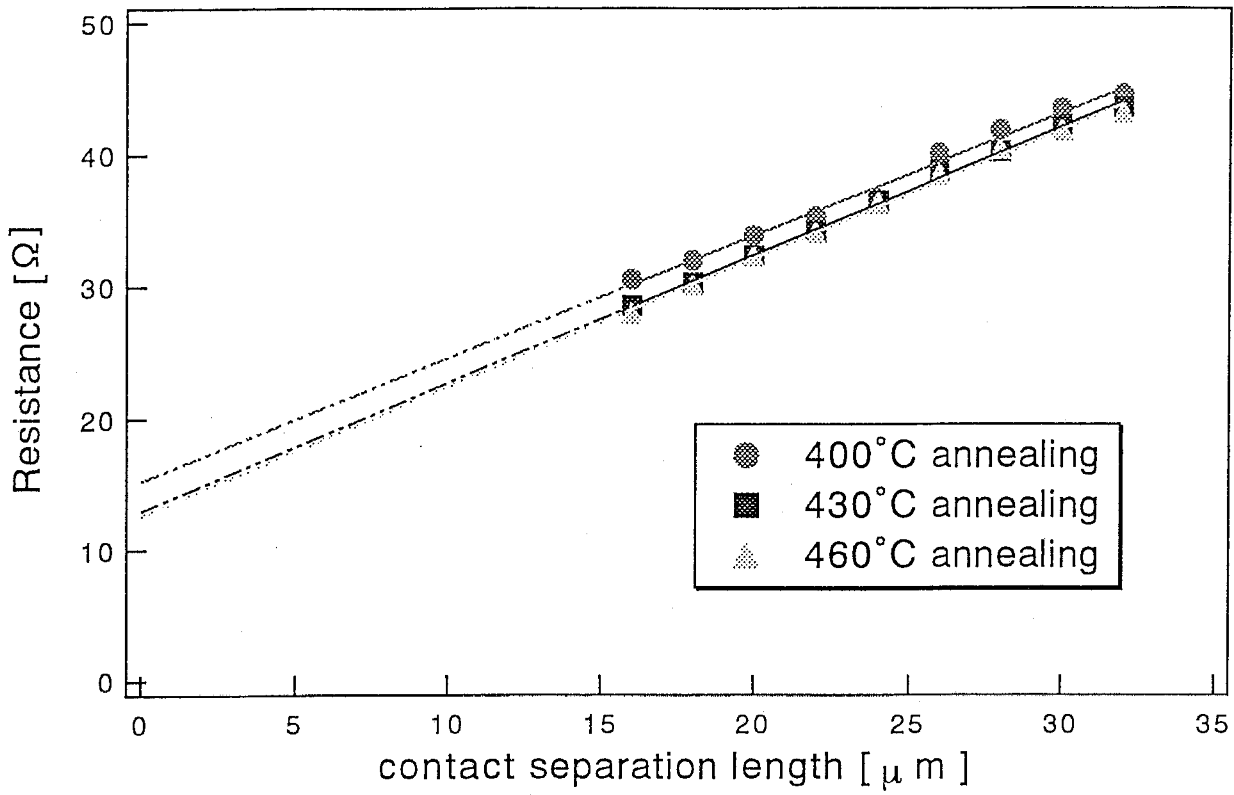

Fig. 6.2 (c) Plot of measured resistance as a function of contact separation length (Zn/Au).

Table 6.1 Contact and sheet resisitivity.

Ref.
Sheet resistivity measured by Van der Pawu method: 2.11×10^{-2} ($\Omega \cdot$cm)

Table (a)-1. Mn/Au applied voltage=1[V]

annealing Temp. (°C)	ρ_c [$\Omega \cdot$cm]	ρ_s [$\Omega \cdot$cm]
380	3.57±0.33 ×10	1.34±0.29 $\times 10^{-2}$
400	3.73±0.16 ×10	1.73±0.13 $\times 10^{-2}$
420	3.42±0.26 ×10	1.95±0.24 $\times 10^{-2}$

Table (a)-2. Mn/Au applied voltage=2[V]

annealing Temp. (°C)	ρ_c [$\Omega \cdot$cm]	ρ_s [$\Omega \cdot$cm]
380	2.72±0.36 ×10	1.45±0.33 $\times 10^{-2}$
400	2.88±0.15 ×10	1.87±0.13 $\times 10^{-2}$
420	2.45±0.24 ×10	2.12±0.21 $\times 10^{-2}$

Table (b). Zn/Au

annealing Temp. (°C)	ρ_c [$\Omega \cdot$cm]	ρ_s [$\Omega \cdot$cm]
400	1.98±0.12 ×10	1.26±0.05 $\times 10^{-2}$
430	1.69±0.06 ×10	1.32±0.03 $\times 10^{-2}$
460	1.64±0.08 ×10	1.33±0.03 $\times 10^{-2}$

Table (c)-1. Ti/Pt/Au applied voltage=1[V]

annealing Temp. (°C)	ρ_c [$\Omega \cdot$cm]	ρ_s [$\Omega \cdot$cm]
380	2.69±0.55 ×10	1.69±0.23 $\times 10^{-2}$
420	3.49±0.39 ×10	1.63±0.17 $\times 10^{-2}$
460	3.88±0.32 ×10	1.34±0.135 $\times 10^{-2}$

Table (c)-2. Ti/Pt/Au applied voltage=2[V]

annealing Temp. (°C)	ρ_c [$\Omega \cdot$cm]	ρ_s [$\Omega \cdot$cm]
380	2.27±0.55 ×10	1.74±0.23 $\times 10^{-2}$
420	3.19±0.66 ×10	1.64±0.28 $\times 10^{-2}$
460	4.06±0.46 ×10	1.58±0.19 $\times 10^{-2}$

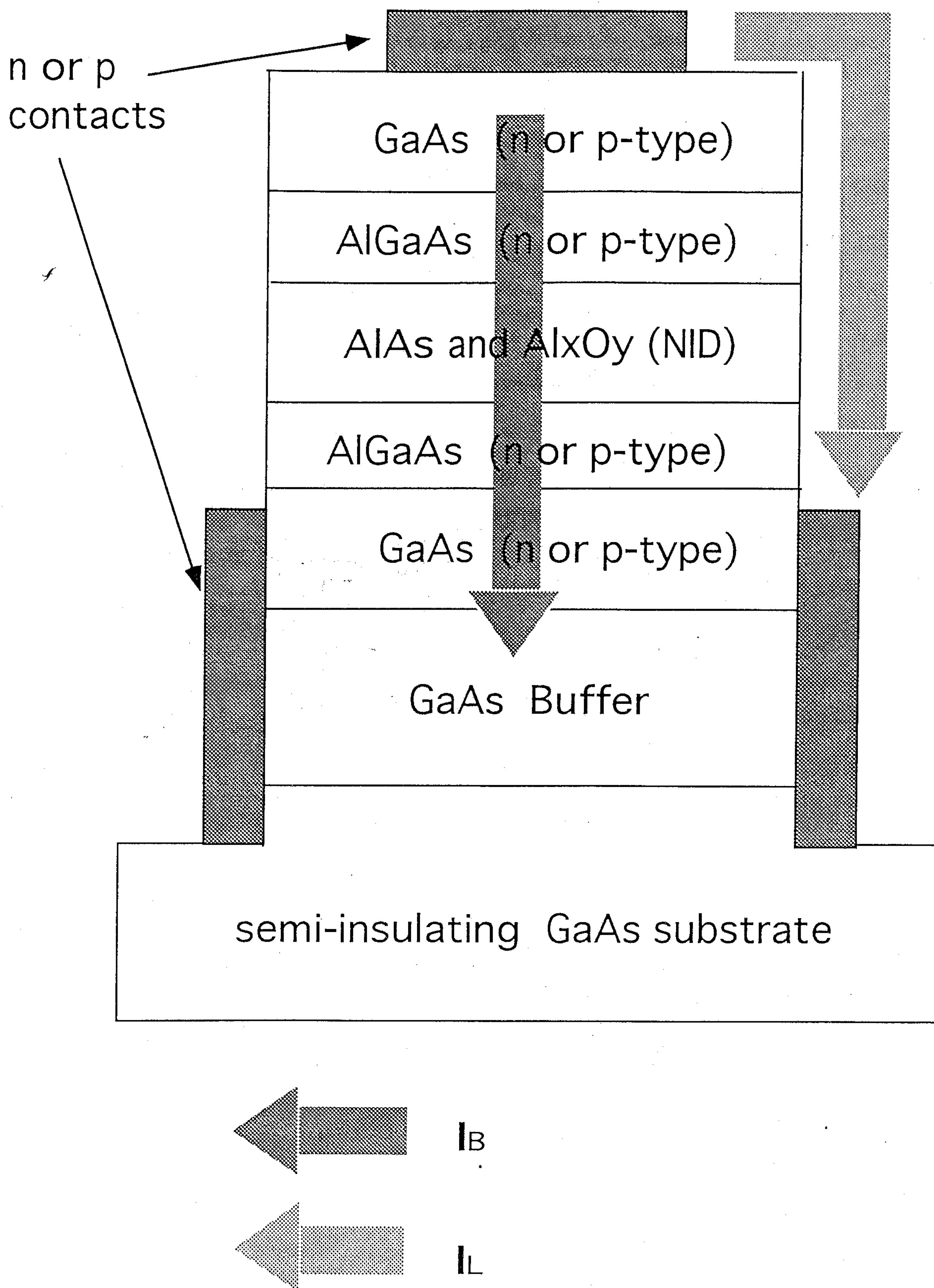

Fig. 6.3 Schematic drawing of structure to evalue electrical characterization of AlxOy.